Delineation and quantification of submerged aquatic vegetation (SAV) in inland lakes using multispectral sensors

MUJEEB-RAHMAN NUHU
February, 2016

SUPERVISORS:
Dr.ir. Mhd. Suhyb Salama
Prof.ing. Wouter Verhoef

Delineation and quantification of submerged aquatic vegetation (SAV) in inland lakes using multispectral sensors

MUJEEB-RAHMAN NUHU
Enschede, The Netherlands, February, 2016

Thesis submitted to the Faculty of Geo-Information Science and Earth Observation of the University of Twente in partial fulfilment of the requirements for the degree of Master of Science in Geo-information Science and Earth Observation.
Specialization: Water Resources and Environmental Management

SUPERVISORS:
Dr.ir. Mhd. Suhyb Salama
Prof.ing. Wouter Verhoef

THESIS ASSESSMENT BOARD:
Prof. Dr. Z., Su (Chair)
Ir., G.W.A.M., (Guido) Waajen (External Examiner, Waterboard Brabantsedelta, The Netherlands)

ABSTRACT

Inland lakes provide great variety of services in the Netherlands. This is evident by the numerous lakes created by the Dutch at various sections of their cities. In-situ underwater and above water radiometric measurements were done at different lakes between September, 2015 and October, 2015 using TriOs RAMSES sensors. Water samples were also taken at different points of measurements for the different lakes and later analysed in the laboratory following standard water quality measurement protocols. The in-situ radiometric measurements were used in computing above water remote sensing reflectance (Rrs), underwater remote sensing reflectance (r_{rs}) and diffuse attenuation coefficient (K_d). In-situ derived K_d values ranged from 0.027-13.675 m^{-1} in Binnenschelde, 0.215-23.099 m^{-1} in Markiezaatsmeer, 0.030-11.971 m^{-1} in Hulsbeek and 0.139-19.867 m^{-1} in Kristalbad. The Spectral Angle Mapper (SAM) method was used for the delineation of Submerged Aquatic Vegetation (SAV) using spectral libraries of field collected end members of SAV in the Binnenschelde Lake. An overall accuracy of 89.53% was obtained when ground truth regions of interest were used to assess the accuracy of the classification. The spatiotemporal variability of SAV was then analysed and Normalised Difference Vegetation Index (NDVI) was explored to estimate the extent and abundance of SAV coverage. After the SAM classification of SAV, linear spectral unmixing was performed to ascertain the fractions of pure and mixed pixels of SAV and water in the multispectral images. Inherent Optical properties (IOPs) of the lakes were derived using the laboratory measured water quality variables. The contribution of bottom reflectance was highly significant because the lakes were optically shallow. Derived IOPs (total absorption coefficient (a) and total backscattering coefficient (b_b)) were used in computing the bottom reflectance (r^B_{rs}), water column reflectance (r^C_{rs}) and bottom albedo (ρ) of each lake at each site. Attenuation coefficient of Photosynthetically Active Radiation (K_d(PAR)) was also derived from the in-situ radiometric measurements. Using K_d(PAR), the euphotic depth (Z_{eu}) of each lake was then computed. Z_{eu} ranged from 1.16 to 2.93, 0.53 to 2.59, 1.42 to 6.12 and 1.51 to 1.79 m for Binnenschelde, Markiezaatsmeer, Hulsbeek and Kristalbad respectively.

Keywords: Remote sensing, Submerged Aquatic vegetation, Diffuse attenuation coefficient, Euphotic depth, water quality, Inherent optical properties, Multispectral.

ACKNOWLEDGEMENTS

First and foremost, I thank the Almighty Allah for granting me the opportunity and ability to pursue this program successfully. I wish to also thank the Ghana Education Trust Fund (GET fund) for providing me the financial support to pursue my study.

My sincere gratitude goes to my first supervisor, Dr.ir. Mhd. Suhyb Salama who guided and assisted us in carrying out the field measurement and the Msc research. For your patience in guiding us throughout this research, may Allah richly bless you. I thank Prof. ing. Wouter Verhoef for his guidance, advice and constructive criticisms. I would like to thank the Vechtstromen and Brabantsedelta Water Boards for their support. In particular I am indebted to Arjan Segeren, Guido Waajen from the Brabantsedelta, Sjon Monnix and Leontien van der Molen from Vechtstromen and Bas Waanders, Park manager of Het Hulsbeek for providing the sampling boats and facilitating the field works. I would like to thank the Netherlands Space Office (NSO) for providing SPOT-6 images through the Satellite Data Portal. I appreciate the support of the United States Geological Survey (USGS) who freely provided the Landsat 8 OLI images for this study.

My heart felt gratitude goes to Dr. Suhyb Salama once again and Dr. C.M.M Mannaerts for your assistance in preparing the Geo-Information Science Laboratory and setting up our apparatus for the analysis of our water samples. I thank the entire staff of the department of Water Resources and Environmental Management of the Faculty of Geo-Information Science and Earth Observation, University of Twente for the great effort put in my entire study.

For my lovely wife, I sincerely thank you for your patience, support and prayers throughout this challenging period. May Allah richly bless you. I thank my siblings and the rest of my family members for their prayers also. Finally, I thank my colleague students and friends for their advice and encouragement especially when the going was very tough. I greatly cherish all your support. May Allah bless the knowledge we have acquired.

TABLE OF CONTENTS

LIST OF FIGURES

LIST OF TABLES

LIST OF SYMBOLS

a	Total absorption coefficients
b_b	Total backscattering coefficients
D_B	Distribution function (scattered photons from water bottom)
D_c	Distribution function (scattered photons from column of water)
E_d	Downwelling irradiance
E_{d+0}	Downwelling irradiance above the surface of the water
E_{d-z}	Downwelling irradiance below the surface of the water
H	Depth of water bottom
K	Sum of attenuation coefficients ($a + b_b$)
K_d	Diffuse attenuation coefficient
K_d (PAR)	Diffuse attenuation coefficient of photosynthetically active radiation
L_u	Upwelling radiance
L_{d_sky}	Downwelling sky radiance
θ	Surface viewing angle from nadir
θ_w	Surface solar zenith angle
R_{rs}	Remote sensing reflectance above the surface of the water
r_{rs}	Subsurface Remote sensing reflectance (under water RS reflectance)
r_{rs}^{c}	Subsurface Remote sensing reflectance of water column
r_{rs}^{B}	Subsurface Remote sensing reflectance of bottom of water
r_{rs}^{dp}	Remote sensing reflectance for optically deep water
α	Spectral angle
ρ	Bottom albedo
Z_{eu}	Euphotic depth

LIST OF ABBREVIATIONS

CDOM	Coloured Dissolved Organic matter
DN	Digital Number
GPS	Global Positioning System
MSI	Multi-spectral Instrument
NDVI	Normalised Difference Vegetation Index
OLI	Operational Land Imager
RS	Remote Sensing
RSR	Relative Spectral Response
SAM	Spectral Angle Mapper
SAV	Submerged Aquatic Vegetation
SPM	Suspended Particulate Matter
QUAC	Quick Atmospheric Correction
UAV	Unmanned Aerial Vehicle
SF	Spectral function
USGS	United States Geological Survey
ESA	European Space Agency
NTU	Nephelometric Turbidity Units

1. INTRODUCTION

1.1. Research Problems

(a) The spatial extent and density of SAV in the Binneschelde Lake are largely unknown.
(b) Challenges of RS methods in recognizing SAV in shallow inland lakes.
(c) The euphotic depth of each lake is also unknown.

1.2. Research Objective

The main objective of this study is to detect, delineate and quantify submerged aquatic vegetation (SAV), analyse their spatiotemporal variability using in-situ radiometric measurements and multi-spectral sensors in the Binnenschelde, the Netherlands.

1.2.1. Sub-objectives

The sub-objectives of this research are to;

- Derive Inherent Optical Properties (IOPs) using in-situ radiometric measurements as well water quality variables of optically shallow inland waters in the Netherlands.
- Investigate the bottom albedos and contribution of bottom reflectance of optically shallow inland waters.
- Derive euphotic depths of inland waters using in-situ radiometric measurements.

1.3. Background

Submerged aquatic vegetation (SAV) are rooted plants that grow only in shallow water to allow sufficient light harvesting without emerging from the water surface. Aquatic vegetation influences physical, chemical and biological processes in water bodies and affects the services of aquatic ecosystem (Shekede et al., 2008). SAV in particular provides an important source of food and habitat to small fish, shellfish and many other species (for example birds). SAV also contributes to improving water clarity by absorbing nutrients, producing oxygen and trapping suspended sediment in the water and preventing resuspension of bottom sediments (Pu et al., 2012). However, there is reported decline of SAV in the Netherlands (Giesen et al., 1990). Therefore, for efficient management of aquatic ecosystem in shallow water, there is the need for accurate knowledge of SAV distribution and abundance (Diaz et al., 2004; Jones et al., 2009).

The use of conventional methods lack the spatial representativeness of SAV distributions limiting the optimized management of inland waters (Zhao et al., 2012). Most managers of water bodies are only able to locate SAV on point basis without any information on their spatial extent. The use of aerial photography (Stankelis et al., 2003; Meehan et al., 2005; Rybicki & Landwehr, 2007) in mapping SAV on a large scale is highly labour intensive, time consuming and inaccurate. According to Yuan & Zhang (2008), this is due to the restrictions in working in aquatic environments and difficulty in taking enough samples in larger water bodies. Spatial detection of the extent, density and diversity of SAV is by far the major challenges facing the Water Board of Brabantsedelta in managing the Binnenschelde Lake, the Netherlands.

Remote sensing (RS) techniques have proven to be highly effective in monitoring and assessing the spatial extent as well as abundance of submerged aquatic weeds, though more effective in mapping terrestrial vegetation (Silva et al., 2008; Hunter et al., 2010). The increase in spatial resolution of multi-spectral sensors makes them even more effective for the fine scale detection of SAV (Schmidt & Witte, 2010). However, to be useful, remote sensing methods should provide accurate representation of the inherent spatial heterogeneity of SAV and be repeatable over space and time (Hestir et al., 2008). The major challenge in mapping SAV with remote sensing (RS) techniques is light attenuation in the water due to phytoplankton which could resemble the spectral signature of SAV (Gilvear et al., 2007). Another challenge is discriminating SAV from above water aquatic vegetation.

A number of studies have been conducted to assess the feasibility of using RS in mapping the spatial extent and density of SAV. Valley et al., (2005) evaluated the use of interpolation techniques in mapping the percentage of water volume occupied by submerged aquatic vegetation in three lakes in the USA. Aerial photographs have also been widely used in the delineation of SAV (Kirkman, 1996; Orth et al., 2000) and further quantifying their density with time. Also, Visser et al., (2013) investigated the possibility of using optical remote sensing for the detection and mapping of SAV with spatial and textural information, as well as the possibility of discriminating different species of SAV.

Azzella et al., (2013) used current (in situ measurements) and historic (from previous studies) data in detecting changes in aquatic plants species richness, distribution and occurrence in the last century in the Italian volcanic lake system, central southern Italy. Again, Flynn & Chapra (2014) used Unmanned Aerial Vehicle (UAV) in mapping the spatial distribution of SAV in Clark Fork river, western Montana. A series of RS images with spatial resolutions of 30m were collected and used by Luo et al., (2015) to map the distribution of different types of aquatic vegetation in the Taihu lake, China. However, in terms of comparatively analysing field spectral characteristics alongside remotely sensed images, there is still a lot to explore.

The aim of this research was to detect, classify and quantify SAV in the Binnenschelde Lake using Multispectral Sensors. Spectral Angle Mapper (SAM) algorithm (Boardam et al., 1994) was used in a supervised classification of SAV. Normalised Difference Vegetation Index (NDVI) by Rouse et al., (1974) was explored to estimate the spatial extent and density of the SAV. For all the study areas, Inherent Optical properties (IOPs) were derived from in-situ radiometric measurements. Euphotic depths (Z_{eu}) were also investigated using the attenuation coefficients of photosynthetically active radiation ($K_d(PAR)$) in each study area. The structure of this thesis work is outlined in figure 2.

Figure 1. Submerged Aquatic Vegetation in Binnenschelde

1.4. Research Questions

(a) What is the spectral signature of SAV in the Binnenschelde Lake?
(b) What is the impact of turbidity and attenuation coefficient on the spatiotemporal distribution of SAV in the Binneschelde?
(c) Can we derive IOPs from in-situ radiometric measurements in inland waters?
(d) What are the euphotic depths of the lakes?

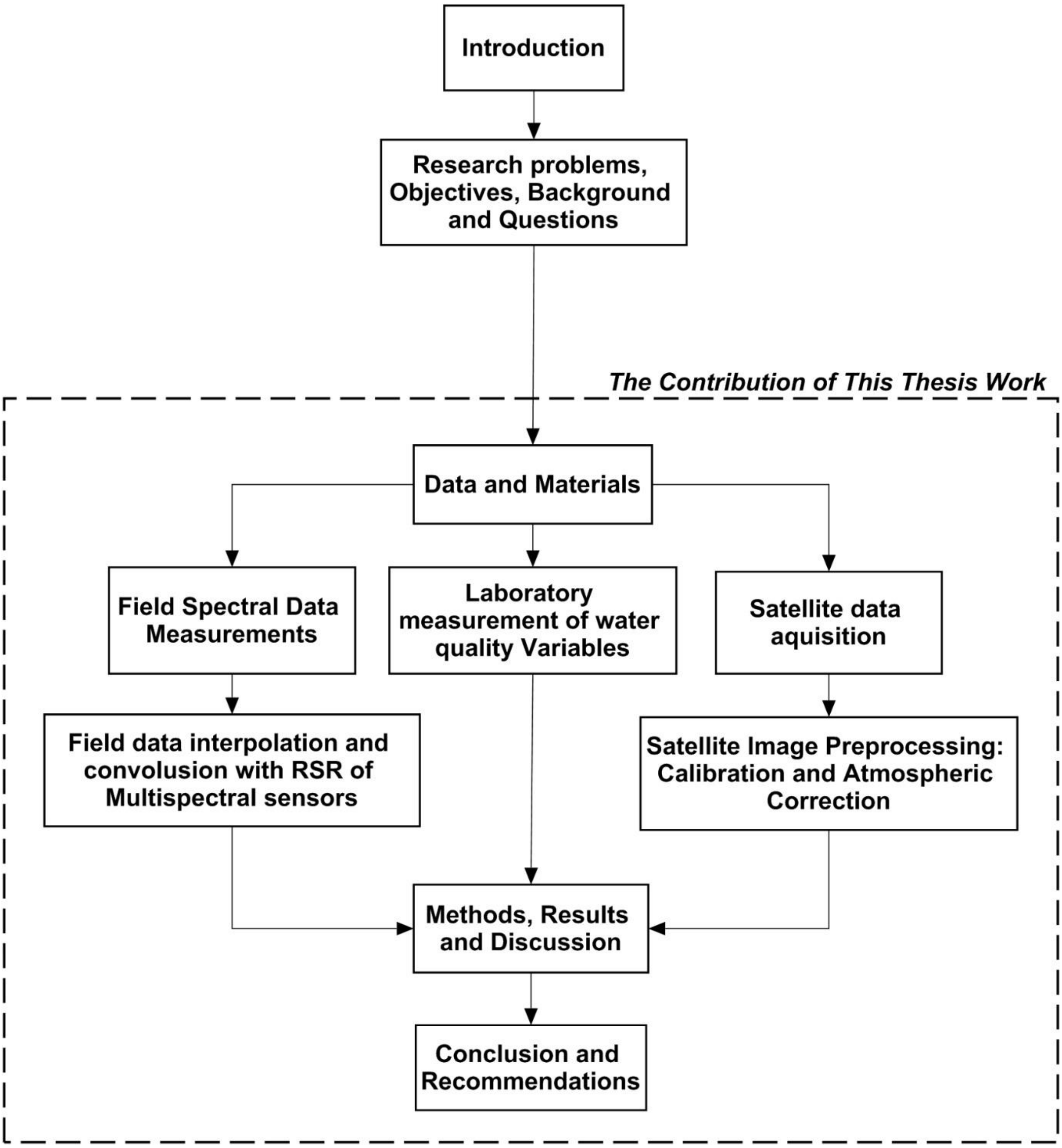

Figure 2. Outline of thesis work.

2. STUDY AREAS

2.1. Binnenschelde and Markiezaatsmeer

Binnenschelde is located in the south-western part of the Netherlands (approximately at N 51º 29'; E4º17' WGS 1984 Geographic) and relatively small compared to Markiezaatsmeer. It borders the residential area of Bergen op Zoom and separated from Markiezaatsmeer Lake by Plaatvliet. According to Gulati & Van Donk (2002), Binnenschelde has a surface area of about 1.78 km^2, with an average depth of 1.5 m and a maximum depth of 3.5 m. It was created within the Eastern Scheldt estuary in the South West Province of Zeeland for the purpose of recreation.

Markiezaatsmeer on the other hand is located approximately at N 51º 29'; E4º17' WGS 1984 Geographic and separated from the Oosterschelde Estuary by the Scheldt Rhine Canal; it has a surface area of about 18 km^2, and 3.9 km^2 of marshes. Markiezaatsmeer has an average depth of 2.1 m and a maximum depth of 3.0 m. Its soil has transformed from Pleistocene to Holocene soils; a unique situation that is rarely found (Tosserams et al., 2001). One of the major challenges for the authorities of both Binnenschelde and Markiezaatsmeer has been water quality management. Since 1996, the concentrations of nitrogen and phosphorus compounds are much higher than the national limits (Withagen, 2000). The spatial detection of SAV is by far the major challenge facing the Water Board Brabantse Delta in managing the Binnenschelde lake. This is because the growth of aquatic plants is triggered by excessive nutrient loading of water bodies (Kiage & Walker, 2009). Figure 3 shows SPOT 6 image of Binnenschelde (A) and Markiezaatsmeer (B).

2.2. Hulsbeek and Kristalbad

Hulsbeek is an artificial lake created mainly for recreation. It is located at latitude 52.181 and longitude 6.530 (WGS 1984 Geographic) in the province of Overijssel, the Netherlands. According to Abbenhues (2003), Hulsbeek is included in the top three most visited lakes in that province; it has a surface area of 250,000 m^2 hectares and a maximum depth of 6 m. Swimming, surfing and playing of several other games usually take place there. For this reason, water quality is of great importance to the management of Hulsbeek.

Kristalbad is an artificially created wetland on the border of Enschede and Helgelo, north of the Twente canal, the Netherlands. Kristalbad can be found approximately at 52^0 14' N; 6^0 49' E (WGS 1984 Geographic) with a surface area of about 400,000 m^2 and 187,000 m^2 area for water storage. This wetland was created in 2002 for water purification and recreation. Figure 4 shows SPOT 6 image of Hulsbeek.

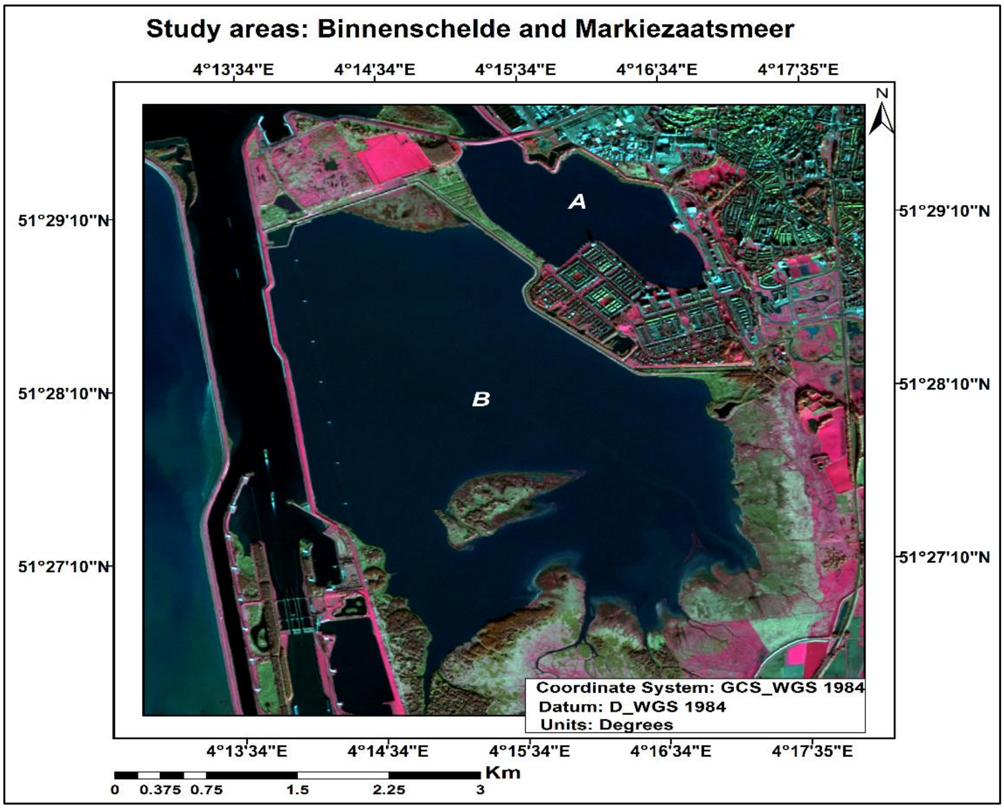

Figure 3. Spot 6 image showing the location of Binnenschelde (A) and Markiezaatsmeer (B). Source (SPOT 6, 12th December, 2015).

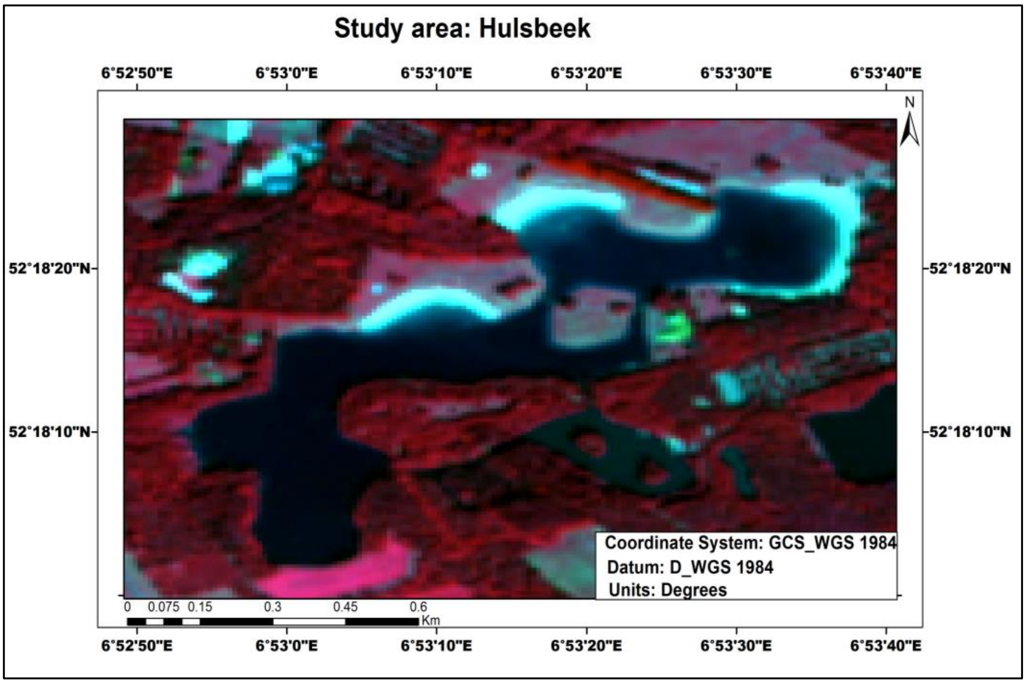

Figure 4. Location map of Hulsbeek. Source (SPOT 6, 12th December, 2015).

3. DATA SETS

3.1. Field Measurements

Field measurements were carried out in the four water bodies from 24th September, 2015 to 1st October, 2015. Days of field measurements were selected based on suitable weather conditions and time of satellite overpass was also taken into consideration. The number of points sampled for each water body was dependent on the size of the water body. Motor boats were used to cruise the water bodies in the sampling process except for the Kristalbad wetland. A total of 51 points were sampled. The position for each sample point was recorded using a hand-held GPS receiver unit. The measurements are summarised in table 1. Sample points were selected to cover the whole water body in order to obtain a representative sampling. For each sample site, spectral measurements and in-situ water quality variables measurements were done. Water samples were also taken for 22 of the sample points. The sampling bottles used were wrapped with aluminium foils to avoid interaction of light with the water samples. After taking the each water sample, a few drops of magnesium carbonate ($MgCO_3$) were added to it to avoid the degradation of the chlorophyll content and help preserve the samples.

Table 1. Summary of field measurements in the study areas.

Study area	Type of Water body	No. of points sampled	No. of water samples taken	Date of measurement	Period of measurement (CET)
Binnenschelde	Lake	14	4	24/09/15	12:01 pm to 15:06 pm
Markiezaatsmeer	Lake	20	6	25/09/15	10:09 am to 13:30 pm
Hulsbeek	Lake	11	6	28/09/15	11:41 am to 12:46 pm
Kristalbad	Wetland	6	6	01/10/15	11:21 am to 13:24 pm

Sampling at Kristalbad wetland was done only at the banks of the ponds because of limited access given to us by authorities of the wetland. The locations of field sampling points for each study area are shown in figure 5.

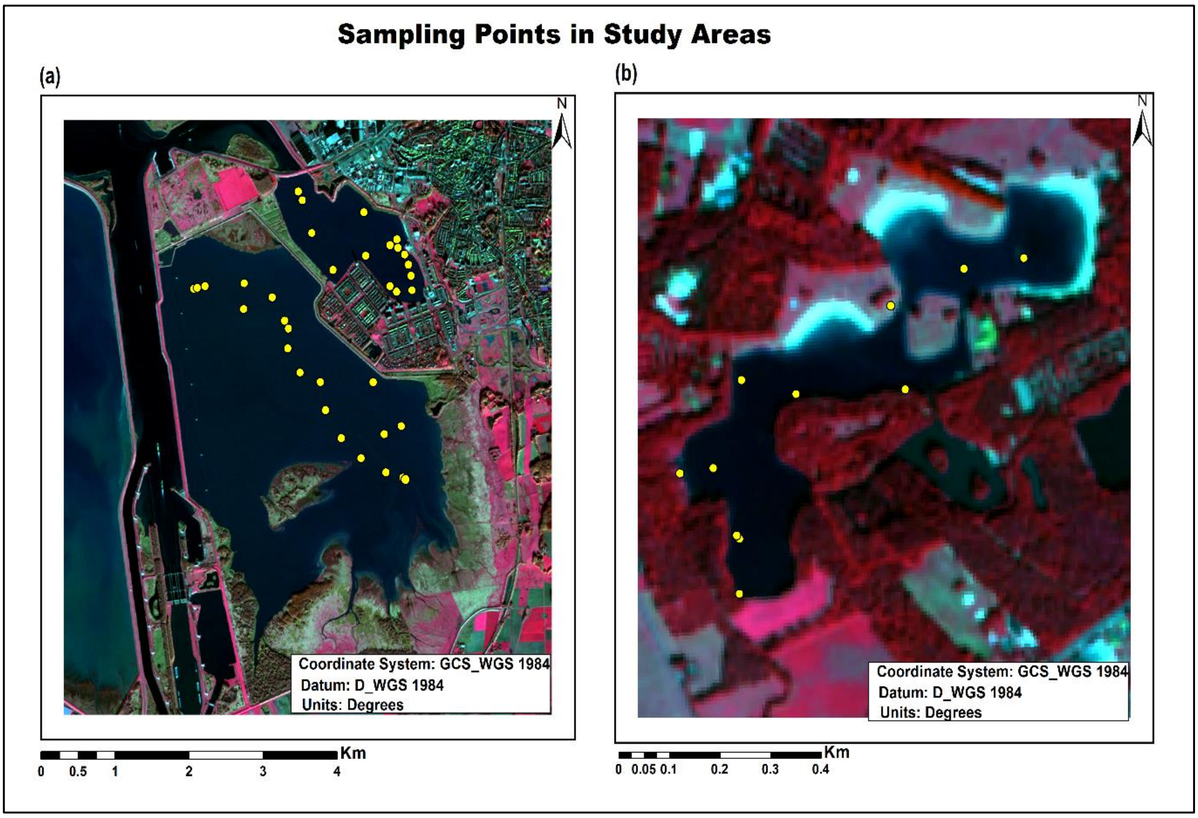

Figure 5. Locations of points sampled (yellow dots) in Markiezaatsmeer & Binnenschelde (a) and Hulsbeek (b). Source (SPOT 6, 12th December, 2015).

3.1.1. Spectral Data Measurement

For each sampling location, radiometric measurements were performed using three TriOs RAMSES sensors. One sensor measured the downwelling irradiance *($E_d(\lambda)$)* from the sun and the sky, and another sensor measured the upwelling radiance ($L_u(\lambda)$) from the target. The third sensor measured microFlu-CDOM at each point in µg/l. Both the radiance and irradiance sensors measure a spectral range from 318 to 951 nm with a sampling interval of 3.3 nm. Downwelling irradiance beneath the water surface and at different depths was also measured in order to quantify the light intensity and the attenuation coefficient of the water. Measurements were done with precaution. Water surfaces with shadows cast on them or specular reflectance were avoided as much as possible. Figure 6. Shows how measurements were done in the field.

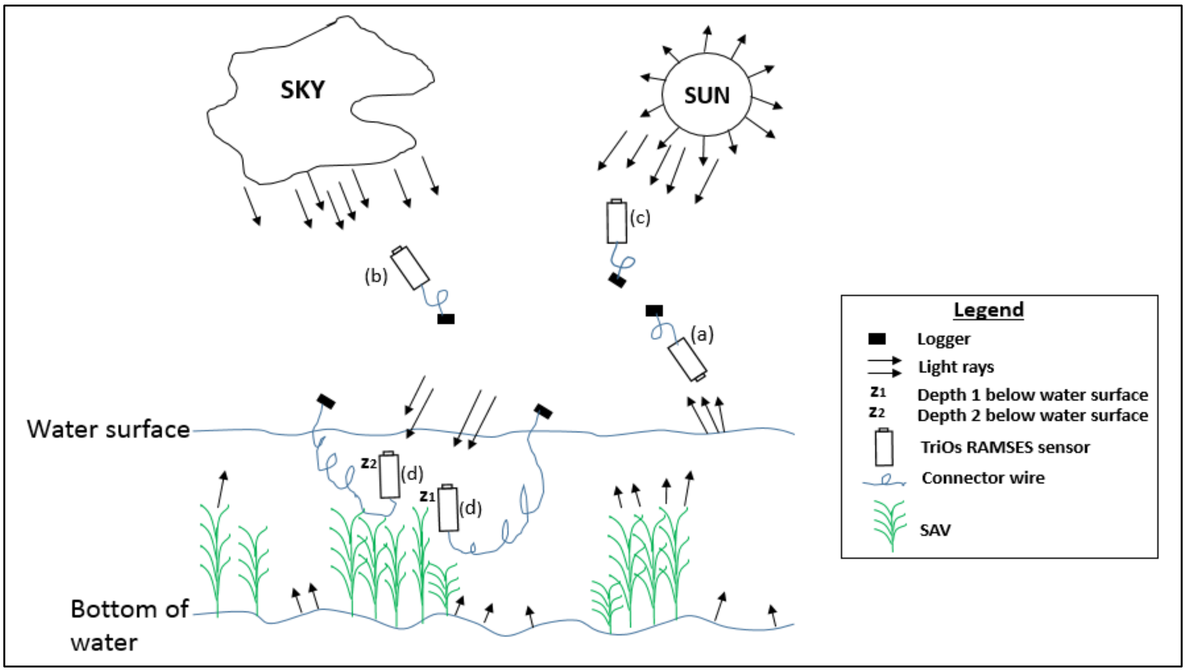

Figure 6. Schematic representation of radiometric measurements carried out in the field.

Where:

(a) is upwelling radiance above the water surface (L_u+0), (b) downwelling sky radiance (L_d_sky), (c) downwelling irradiance (E_d+0), (d) underwater downwelling irradiance at different depths (z_1 and z_2) just above SAV (E_d-z).

3.1.2. In-situ measurement of water quality variables

Water quality variables were also measured in-situ using HACH HQ40d multi-parameter-meter. These are the water body temperature, pH and dissolved oxygen at each sample point. At some sampling points, water surface temperature (WST) was also measured with a hand held Testo 830-T2 thermometer.

3.2. Laboratory Measurement of water Quality Variables

Water samples collected were put in a refrigerator at a temperature of 5°C. All samples were analysed for Suspended Particulate matter (SPM), Chlorophyll a, Turbidity and Coloured Dissolved Organic matter (C-DOM). Analysis of all samples was done at the Geo-Information Science Laboratory of the Faculty of Geo-Information Science and Earth Observation, University of Twente, the Netherlands.

3.2.1. Suspended Particulate Matter

Gravimetric analysis method was used in measuring the Suspended Particulate Matter (SPM). The setup (see figure 7) used for the measurement of SPM consist of: Sartorius 1872 electronic balance (highly sensitive and measures four digits after the decimal place), petri dish, Whatman GF/F filters (pore size of 0.45 μm), vacuum pump, filtration system, graduated cylinders, forceps (used to handle filter and petri dish), oven and distilled water. Each dry Whatman glass fibre filter was weighted with the electronic balance twice and the average taken as the dry weight of the filter. Volumes of water samples filtered are 25 ml for less turbid samples (relatively clear water) and 20 ml for turbid samples. After filtration of each sample, the filtrate with the filter was put in the oven overnight to dry at a temperature of 105^{o} C. When the filter was finally removed from the oven, it was cooled at room temperature and the final weight taken again. To obtain the total suspended solids in mg/l, eq. (1) was used.

$$Total\ suspended\ solids\left(\frac{mg}{l}\right) = \frac{final\ weight\ (mg) - initial\ dry\ weight\ (mg) * 1000}{sample\ volume\ (ml)} \tag{1}$$

(a) (b) (c)

Figure 7. Laboratory setup; (a) Filtration system, (b) filters in oven, (c) Electronic balance.

3.2.2. Chlorophyll a concentration

Absorption of chlorophyll a was measured using chlorophyll a measurement protocol adapted by Elizabeth J. Arar (U.S.Environmental Protection Agency, 1997). Collected samples were filtered using whatman glass fibre (G/F) filters of 0.45 µm pore sizes and 55mm diameter to extract phytoplankton pigments. Relatively clear samples were filtered using 70 ml whiles the turbid samples were filtered using different volumes ranging from 40 ml to 60 ml. Petri dishes were used to transport the sample with forceps. 90% acetone (has high efficiency in extracting chlorophyll a from most types of algae) was used as extraction solvent. The filters with filtrates were grinded using a tissue grinder and pestle. Following the measurement protocol, a total volume of 10 ml of 90% acetone was used to dissolve and dilute each grinded filter. The grinded filter with 10 ml acetone was transferred to centrifuge tube and centrifuged for 5 minutes at speed of 1000 rpm. The extract was then clarified by the centrifuge. For each extract, 2 ml was transferred to a cuvette of optical path length 1cm. The cuvette was put in a spectrophotometer (UV-6300PC) and scanned at selected wave lengths (750 nm, 664 nm, 647 nm and 630 nm). A general scan from 300 nm to 1100 nm wave length range at an interval of 1 nm was also done separately to analyse the absorbance of each sample at those wave lengths. Jeffrey and Humphrey's Trichromatic equations (Eq. 2) were used to calculate the concentration (mg/L) of chlorophyll *a* in the extraction solution analysed. To obtain this, the absorbance value at 750 nm was first subtracted from the absorbance at 664 nm, 647 nm and 630 nm to obtain 750 nm corrected absorbance values. The corrected values were then put in eq. (2).

$$C_{E,a} = 11.85(Abs\ 664) - 1.54(Abs\ 647) - 0.08\ (Abs\ 630) \qquad (2)$$

Where:
C_{Ea}= concentration (mg/L) of chlorophyll a in the extraction solution analysed
Abs 647= corrected absorbance of 647 nm
Abs 664= corrected absorbance of 664 nm
Abs 630= corrected absorbance of 630 nm
To finally calculate the concentration of chlorophyll a pigment in the whole sample, a generalized equation (eq. (3)) was used.

$$C_s = \frac{C_{E,a}\ \ X\ \ extract\ vlume\ (L)\ X\ DF}{sample\ volume\ (L)\ X\ cell\ length\ (cm)} \qquad (3)$$

Where:

C_s= concentration (mg/L) of pigment in water sample. In this case, the concentration of chlorophyll-a pigment in the sample.
Extract volume= volume (L) extracted before dilution was done (typically 0.0104)
Cell length= optical path length (cm) of cuvette used (1cm=0.01m in this case)
Sample= whole volume (L) of sample that was filtered
DF= the dilution factors used.

(a) (b)

Figure 8. (a) Spectrophotometer (UV-6300PC), (b) Sample scan in the spectrophotometer.

3.2.3. Turbidity

In the laboratory, HACH 2100P Turbidimeter was used to measure turbidity of the water samples. This measures in NTU (Nephelometric Turbidity Units) and was set to automatic range and signal averaging mode. Calibration was done with three standards provided (see figure 9). These are Gelex Second Turbidity Standard 0-10 NTU, 10-100 NTU and 100-1000 NTU. The sample cell was filled to the line with the water sample. Before inserting each sample cell, it was cleaned with two drops of silicon oil and a soft lint-free cloth provided to increase the accuracy of measurements. Readings of each sample were carefully taken five times after which the average reading was recorded as the turbidity of that sample.

(a) (b)

Figure 9. (a) Gelex Second Turbidity Standards, (b) HACH 2100P Turbidimeter.

3.2.4. Coloured Dissolved Organic Matter

Apart from the in situ measurement of CDOM with the TriOs RAMSES sensor, CDOM which is also known as yellow substances or Gelbstoff was also measured in the laboratory. Filtering of water samples was done with whatman G/F filters (0.45 µm pore size, 55 mm diameter). A second filtering was done using a 0.2 µm filter and string. One filter was used for each sample. The string was however cleaned thoroughly with distilled water before filtering each sample. After filtration was done, 2 ml of each sample was transferred to a cuvette of optical path length 1 cm for scanning in the spectrophotometer (UV-6300PC). A fixed wavelength (440 nm) scan was done after which a general wave length (300nm to 1100nm) scan at an interval of 1 nm was also done. A blank distilled water sample was also scanned at 440nm. Before each scan, the cuvette was cleaned with lint free wipes. The spectral absorption coefficient of the CDOM was calculated from the measured absorbance using eq. (4). Absorbance of the blank ($A_{blank}(440)$) was subtracted from the absorbance of each sample at 440nm.

$$a^*(\lambda) = 2.303\, A(\lambda)/l \tag{4}$$

Where:

$a^*(\lambda)$ =Spectral absorption coefficient of CDOM

A(λ) =corrected absorbance value of CDOM ($A(440)$- $A_{blank}(440)$)

l=optical length of cuvette=1cm

3.2.5. Lansat-8 OLI and SPOT 6 MS Data set

Landsat-8 Operational Land Imager (OLI) images were downloaded from (http://earthexplorer.usgs.gov/) for a period of April 1, 2015 to October 31, 2015. This period returned six (20% cloud cover) images covering Binnenschelde and Markiezaatsmeer study areas only. The other two study areas were left out because of the relatively course spatial resolution of Landsat 8 OLI spectral bands. The spectral bands of Landsat 8 Oli and their wavelengths are shown in table 2 (http://landsat.usgs.gov/band_designations_landsat_satellites.php).

Table 2. Landsat 8 OLI spectral bands and Wavelengths.

Bands	Wavelength (micro meters)	Resolution (meters)
Band 1 - Coastal aerosol (OLI)	0.43 - 0.45	30
Band 2 – Blue (OLI)	0.45 - 0.51	30
Band 3 – Green (OLI)	0.53 - 0.59	30
Band 4 – Red (OLI)	0.64 - 0.67	30
Band 5 - Near Infrared (NIR) (OLI)	0.85 - 0.88	30
Band 6 - SWIR 1 (OLI)	1.57 - 1.65	30
Band 7 - SWIR 2 (OLI)	2.11 - 2.29	30
Band 8 – Panchromatic (OLI)	0.50 - 0.68	15
Band 9 – Cirrus (OLI)	1.36 - 1.38	30
Band 10- Thermal Infrared (TIRS) 1	10.60 - 11.19	100 * (30)
Band 11- Thermal Infrared (TIRS) 2	11.50 - 12.51	100 * (30)

Further processing of the downloaded data was done with standard parameters of the Landsat 8 data products as summarised in table 3.

Table 3. Landsat 8 Standard data product Processing Parameters [UTM, Universal Transverse Mercator; WGS, World GeodeticSystem; OLI, Operational Land Imager; TIRS, Thermal Infrared Sensor]

Product Type	Level 1T (terrain corrected)
Data Type	16-bit unsigned integer
Output format	GeoTIFF
Pixel Size	15meters/30meters/100meters(panchromatic/multispectral/thermal)
Map Projection	UTM (Polar Stereographic for Antarctica)
Datum	WGS 84
Orientation	North-up (map)
Resampling	Cubic convolution
Accuracy	OLI: 12 meters circular error, 90 percent confidence TIRS: 41 Meters circular error, 90 percent confidence

3.2.6. SPOT 6 Multispectral Data set

Spot 6 is a multispectral sensor built by the AIRBUS Defence and space. It was launched on 12th September, 2012. The SPOT 6 multispectral images covering all the study areas were obtained from the Netherlands Space Office through their Satellite data Portal. For Binnenschelde and Markiezaatsmeer, two cloud free images (November 2, 2015 and December 4, 2015) were obtained. Two cloud free images (June 27, 2014 and August 3, 2015) were also obtained for Hulsbeek and Kristalbad. Table 4 shows the four bands of Spot 6, their wavelength ranges and spatial resolution (http://www.satimagingcorp.com/satellite-sensors/spot-6/).

Table 4. SPOT 6 multispectral bands and Wavelengths.

Bands	Wavelength (micro meters)	Resolution (meters)
Band 1 – Blue	0.455-0.525	6.0
Band 2 – Green	0.530-0.590	6.0
Band 3 – Red	0.625-0.695	6.0
Band 4 – Near-Infrared	0.760-0.890	6.0

4. METHODOLOGY

4.1. Image Processing

4.1.1. Atmospheric correction of Landsat 8 OLI images

For accurate investigation of the spectral properties (reflectance) of the earth's surface, atmospheric correction is very crucial because of the absorption and scattering effects of the atmosphere. With atmospheric correction, ground features of an image can better be separated (Sharma et al., 2009). Atmospheric correction of Landsat 8 OLI images was done using the QUick Atmospheric Correction (QUAC) method. Without axillary information, QUAC directly determines the atmospheric compensation parameters from observed pixel spectra (Guide, 2009). This method assumes linear relationship between spectral reflectance and measured radiance similar to the Empirical Line Method (ELM)) using the standard radiance equation (Bernstein et al., 2005a);

$$\rho_j(\lambda) = A(\lambda) + \frac{B(\lambda)}{1-S(\lambda)<\rho(\lambda)>}\rho_j^0(\lambda) + \frac{C(\lambda)}{1-S(\lambda)<\rho(\lambda)>} < \rho(\lambda) > \tag{5}$$

Where: A, B, C and S are coefficients describing the transmission and scattering effects of the atmosphere, ρ_j is the reflectance observed (normalised radiance by the surface normal component of the solar flux) for the j'th pixel at a spectral band with central wavelength λ, ρ_j^0 represents the actual surface reflectance and $<\rho>$ is the surface reflectance that is spatially averaged.

Assuming the conditions that (1) $S<\rho>$ is small and when either, (2) the diffuse and the direct transmittance terms can be combined with a single reflectance variable, or (3) the diffuse and backscattering terms can be combined, then eq. 5 is reduced to a linear form as;

$$\rho_j(\lambda) = A(\lambda) + B(\lambda)\rho_j^0(\lambda) + C(\lambda) < \rho(\lambda) > \tag{6}$$

$$\rho_j^0(\lambda) = \frac{\rho_j(\lambda)-\rho_b(\lambda)}{g_o\sigma\rho(\lambda)} \tag{7}$$

Where: g_o is the normalisation factor and $\sigma\rho$ is the correction factor B. To retrieve the actual surfaces spectral reflectance, eq. 6 is rearranged to obtain eq. 7 using extracted compensation parameters that are in-scene-determined. One advantage of QUAC is that, its approach for retrieving aerosol optical depth does not depend on the presence of dark pixels like most methods do (Bernstein et al., 2005a). According to Bernstein et al., (2005a, 2005b), some previous results prove that QUAC yields very accurate results compared to more sophisticated methods of atmospheric correction.

In ENVI 5.3, each image was loaded using the *_MTL.txt metadata file. With the input raw image, QUAC creates a surface reflectance image that is scaled into two-byte unsigned integers using a reflectance scale factor of 10,000. In order to obtain a reflectance data range from 0-1, ENVI BandMath tool was used to divide the reflectance pixel values by 10,000 using eq. 8. The output reflectance images (see appendix 2) were then used for further processing.

$$\frac{(B1\ le\ 0)*0+(B1\ ge\ 10000)*1+(B1\ gt\ 0\ and\ B1\ lt\ 10000)*float(B1)}{10000} \tag{8}$$

Where: B1 represents each band of the image.

4.1.2. Atmospheric correction of Spot 6 MS images

The method described in section 4.1.1 was also applied to the Spot 6 images. The only difference is that, Spot 6 images were loaded using the DIMAP (.XML) metadata file in ENVI (dim*.xml). Eq. 8 was also used to finally obtain the reflectance data range from 0-1. The output images were then used for further processing.

4.2. Ramses Data Interpolation and Convolution

For accurate comparison of measurements taken by two different sensors, it is crucial to interpolate the measurements of one from the other. This is because of the difference in wavelength interval and range of each sensor. Landsat 8 OLI has wavelength interval of 1 nm while Ramses has an interval of 3.3 nm. Ramses measured in-situ reflectance spectra data was interpolated to obtain new data set in 1 nm interval. The Relative Spectral Response (RSR) of Landsat 8 OLI was then convoluted with the spectral response of the Ramses. The RSR of Landsat 8 OLI, obtained from the web (http://landsat.usgs.gov//instructions.php) is shown in figure 10. Five of the Landsat 8 OLI bands, Coastal Aerosol (CA), Blue, Green, Red and Near Infra-Red (NIR) were convolved with the in-situ reflectance spectra of Ramses using the band equivalent reflectance (BER) equation (eq. (9)). Hence, band-weighted reflectance of Ramses (R_x) were derived for each band and site and used for further analysis. The same process was carried out in convolving the RSR of Spot 6 to the spectral response of RAMSES. However the RSR of Spot 6 could not be obtained. Therefore, the band widths (lower and upper wavelengths) of each band were used to compute a Gaussian spectral response function and taking the Full Width at Half Maximum (FWHM) values of the spectrum curve. The resulting SRF were then convolved with the spectral response of RAMSES to obtain R_x (eq. (9)) for each site.

$$R_x = \frac{\sum_{i=\lambda_{min}}^{\lambda_{max}} r_i \rho_i}{\sum_{i=\lambda_{min}}^{\lambda_{max}} r_i} \tag{9}$$

Where: R_x is the BER for band x, λ_{min} is the minimum value of band x filtration function, λ_{max} is the maximum value of band x filtration function, r_i is the RSR of band x at the wave length i. ρ_i is the interpolated spectral response of Ramses at wavelength i.

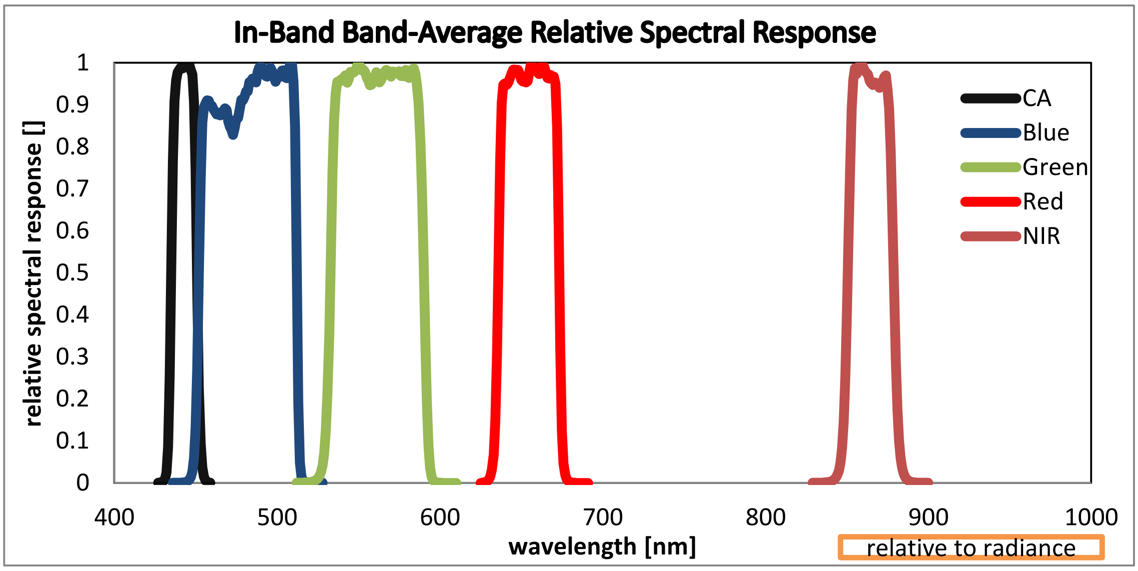

Figure 10. Relative spectral response of Landsat 8 OLI (USGS, 2015).

4.3. Remote sensing Reflectance

For all the study areas, the remote sensing reflectance of each location (Rrs(λ)) was calculated using eq. (10) (J.L. Mueller et al., 2003; Mobley, 2004). It is the ratio of the upwelling radiance (Lu(λ)) to the downwelling irradiance (Ed(λ)) for each point of measurement just above the surface of the water. Rrs is very important in the study of apparent optical properties as it provides significant optical properties of the water constituents (Salama et al., 2009).

$$R_{rs} = \frac{\mathrm{Lu}(\lambda)}{\mathrm{Ed}(\lambda)} \qquad (10)$$

Where: Rrs =water leaving reflectance [sr^{-1}]

Lu(λ) =upwelling radiance just above the surface of the water [mw.nm^{-1}.sr^{-1}]

Ed(λ)) =downwelling irradiance just above the surface of the water [mw.nm^{-1}]

4.4. Underwater remote sensing reflectance

Underwater remote sensing reflectance (r_{rs}) is the ratio of the upwelling radiance to the downwelling irradiance, evaluated just below the surface of the water. This was obtained using eq. (11) (Lee et al., 1999).

$$Rrs \approx \frac{0.5r_{rs}}{1-1.5r_{rs}} \qquad (11)$$

From eq. (11),

$$r_{rs} \approx \frac{R_{rs}}{0.5+1.5R_{rs}} \qquad (12)$$

Eq. (12) was used to compute the values of r_{rs} from the in-situ derived Rrs.

4.5. In-situ attenuation coefficient

As solar radiation is transmitted through water, it interacts with suspended particulate matter as well as dissolved organic matter present in the water (Mobley, 2004). This leads to absorption and/ or scattering of the radiation as it moves down the water column. Using the downwelling irradiance measured at different depths (Z_1 and Z_2), in-situ diffused attenuation coefficient (K_d) was calculated using eq. (13).

$$K_d = -\frac{1}{\Delta Z}\ln\left[\frac{E_d(Z_2)}{E_d(Z_1)}\right]:\ |Z_2| > |Z_1| \qquad (13)$$

Where ΔZ is thickness of the water column [m], E_d is the downwelling irradiance [Wm^2nm^{-1}]. Z_1 and Z_2 are 0.1m and 0.2m respectively.

4.6. SAM Classsification of SAV in Binnenschelde

For all the four study areas described, SAV were visible only in the Binnenschelde Lake. The classification of SAV was done using the Spectral Angle Mapper (SAM) (Boardam et al., 1994). SAM is a supervised image classification technique that classifies an image using known spectral signatures of the classes, i.e. endmembers. The endmembers could be taken from the laboratory (Park et al., 2007) or the field (Curtarelli et al., 2014). It could also be extracted from an image. SAM determines the spectral similarity between the endmembers spectra and the image spectra in each pixel (Kruse et al., 1993). It measures the similarity of a spectrum to an endmember by computing the angle between them, disregarding their relative brightness values (Akkaynak et al., 2013). The higher the spectral angle, the higher the dissimilarity between the pixel spectra (Liu, 2013). Figure 11 shows a representation of endmember and test spectrum of a two band image (band 1 and band 2) in a two dimensional plot. The origin is the darkest point. This means that pixels with the same spectral signature will fall on the same spectral line. However the further they are away from the origin, the more illuminated (brighter) they are. The main disadvantage of this method is that, it is insensitive to illumination (Kruse et al., 1993).The spectral angle (α), is calculated using eq.15.

For this study, spectral libraries were built from field measurements of SAV (field collected end members). After convolving in-situ Rrs with the SRF of Landsat 8 OLI and SPOT 6 MS sensors, the average Rrs values of the SAV (Rrs(SAV)) were taken. Also, the underwater remote sensing reflectance of the SAV (r_{rs}(SAV)) were convolved with the RSF of both satellites. (Rrs(water), Rrs(SAV)) and (r_{rs}(SAV)) were multiplied by pi( ) to convert to albedo assuming an isotropic light field. Eq. 14 was then applied to obtain two classes (field endmembers) used to build the spectral libraries for SAM classification with field observation as a guide.

$$Rrs(water) = Rrs(SAV) - r_{rs}(SAV) \quad (14)$$

Where: Rrs(water) is the convoluted remote sensing reflectance of only water, Rrs(SAV) is the average remote sensing reflectance of the SAV points and r_{rs}(SAV) is the underwater remote sensing reflectance of the SAV. Maximum spectral angles ranged from 0.39-0.42 radians for Landsat 8 images and 0.37-0.38 radians for SPOT 6 images.

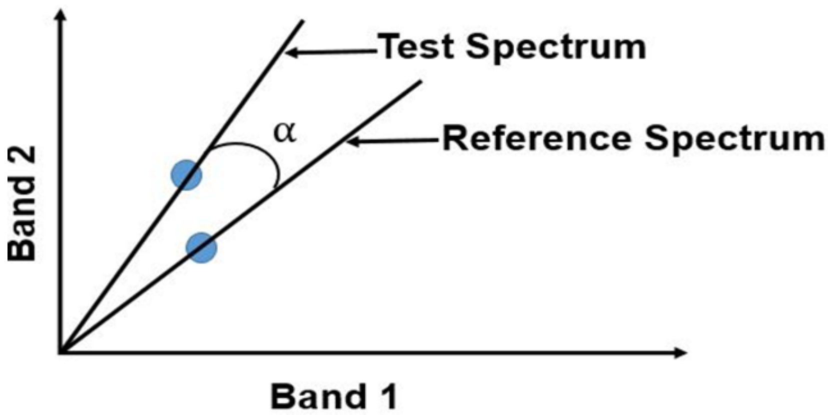

Figure 11. Vector representation of the SAM algorithm for two bands.

Adapted from Kruse et al. (1993).

$$\alpha = cos^{-1}\left(\frac{\sum_{i=1}^{nb} t_i r_i}{\left(\sum_{i=1}^{nb} t_i^2\right)^{1/2}\left(\sum_{i=1}^{nb} r_i^2\right)^{1/2}}\right) \quad (15)$$

Where

α= spectral angle (in radians)
nb= number of bands
t= test (unknown) spectra
r= reference (known) spectra

4.7. Linear Spectral Unmixing of SAV and Water Pixels

In the SAM image classification process, pixels were classified as SAV, water or fractions of SAV and water field endmembers depending or their spectral characteristics. It is therefore crucial to identify pixels that encompass a mixture of both endmembers and their relative abundance in each pixel of the multispectral images. Spectral linear unmixing is decomposition of a measured spectra into its constituent spectra, with fractions indicating the relative abundance of each endmember in the pixel (Keshava & Mustard, 2002) The main principle behind spectral unmixing is that, a data sample vector is assumed to be mixed by the endmembers present in it (Dobigeon et al., 2008). According to Boardman (1989), a linear or nonlinear mixing may occur depending on whether the incident photon goes through a single or multiple scattering before escaping as reflected light. In this study, a linear mixing was assumed to have occurred. The linear spectral unmixing tool in ENVI was used to spectrally unmix the classified multispectral images. A unit sum constraint was assumed. This means that the sum of the fraction of the reflectance of SAV and water is assumed to be equal to 1 for all bands of the image. The linear spectral unmixing was done using ground truth Regions of Interest (ROIs) of the unclassified image.

4.8. Normalised Difference Vegetation Index

Normalised Difference Vegetation Index (NDVI) developed by Rouse et al., (1974), was explored to quantify the abundance of SAV. NDVI was calculated using the reflected solar radiation in the near infra-red (NIR) and red (R) wavelength bands as shown in eq. (24). NDVI is undefined when both wavelengths at NIR and R are zero (Rulinda et al., 2010). Using the Landsat 8 OLI and Spot 6 images of Binnenschelde, NDVI maps were created with ENVI software using the BandMath tool.

$$\mathrm{NDVI} = \frac{\mathrm{NIR}-\mathrm{R}}{\mathrm{NIR}+\mathrm{R}} \tag{16}$$

Band reflectance values were used. Where: NIR is the reflectance at the near infra-red band of Landsat 8 and SPOT 6 whiles R is the reflectance values at the red band of Landsat 8 and SPOT 6.

4.9. Deriving Inherent Optical Properties from In-situ Radiometric Measurements

Inherent optical Properties (IOPs) are the properties of a water constituents that do not depend on the ambient light field that is within the water medium but the water medium only (Mobley, 2004). IOPs include the absorption coefficients of water molecules, phytoplankton pigments, detritus and gelbstoff which make up the total absorption coefficient ($a(\lambda)$). Also the backscattering coefficients of water molecules and suspended particulate matter make up the total backscattering coefficient ($b_b(\lambda)$). ($a(\lambda)$) and ($b_b(\lambda)$) are very important IOPs that influence the propagation of light in a column of water (Salama et al., 2009). Using the measurements of water quality variables described in section 3.2., the total absorption coefficient ($a(\lambda)$) and total backscattering coefficients ($b_b(\lambda)$) were derived from the above water remote sensing reflectance (Rrs) as follows. First of all, Rrs was interpolated to 10 nm wave length interval because of the wavelength intervals of $b_{bw}(\lambda)$ and $a_w(\lambda)$. The underwater remote sensing reflectance was then computed using eq. 12. But from Lee et al., (1999);

$$u = b_b(\lambda)/(\,a(\lambda) + b_b(\lambda)) \tag{17}$$

$$b_b(\lambda) = b_{bw}(\lambda) + b_{bp}(\lambda) \tag{18}$$

$$a(\lambda) = a_w(\lambda) + a_\phi(\lambda) + a_{dg}(\lambda) \tag{19}$$

Where: $b_{bw}(\lambda)$ (m^{-1}) is the backscattering coefficient from Morel (1974) and $a_w(\lambda)$ (m^{-1}) is the absorption coefficient of pure water taken from Pope & Fry (1997). a_ϕ is the absorption coefficient of phytoplankton, $a_{dg}(\lambda)$ is the absorption coefficient of detritus and gelbstoff and $b_{bp}(\lambda)$ is the backscattering coefficient of particulate matter.

Also, $b_{bp}(\lambda) = X\left(\frac{400}{\lambda}\right)^Y$ (20)

Where X=$b_{bp}(400)$=SPM ($b^*_{bp}(400)$)P

400 nm is the reference wavelength. Y is a spectral slope for particulate backscattering reported to be between 0 and 0.25 (Salama & Stein, 2009). $b^*_{bp}(400)$ is the specific backscattering coefficient of SPM at 440 nm and P is the backscattering fraction which was taken as 0.0182 (Petzold, 1972). SPM is the site suspended particulate matter (g/m^3).

$$Y \approx 3.44(1 - 3.17\exp(-2.01\,x)),\ \text{ where } x = \frac{Rrs(440)}{Rrs(490)}$$

$$a_{dg}(\lambda) = G\exp(-S(\lambda - 440)) \quad (21)$$

$$a_{ph} = a^*_{ph}\,[chl\ a] \quad (22)$$

Where G=a^*_{dg}, which is the sum of absorption coefficient of detritus and gelbstoff at 440 nm, S is a spectral slope that is reported to be in the range of 0.011-0.021 nm^{-1} (Carder et al., 1989; Carder et al., 1991). A representative average was taken as 0.015 nm^{-1} (Lee et al., 1999). a^*_{ph} (m^2/mg) is the specific absorption coefficient of phytoplankton taken from Hartmann (1995) and [chl a] is the chlorophyll a concentration (mg/m^3) of the site.

4.9.1. Bottom Albedo of shallow inland Lakes

In shallow waters, the underwater remote sensing reflectance (r_{rs}) signal is made up of the reflectance of constituents in the water column as well as reflectance from the bottom of the water. According to Lee et al., (1999);

$$r_{rs} = r_{rs}^{dp}\left(1 - \exp\left\{-\left[\frac{1}{\cos\theta_w} + \frac{D_u^C}{\cos\theta}\right]\kappa H\right\}\right) + \frac{1}{\pi}\rho\exp\left\{-\left[\frac{1}{\cos\theta_w} + \frac{D_u^B}{\cos\theta}\right]\mathrm{K}H\right\} \quad (23)$$

However, D_u^c, D_u^B and r_{rs}^{dp}, are all functions of u (eq. 17) and were computed as follows (Lee et al., 1999);

$$D_u^c \approx 1.03(1 + 2.4u)^{0.5} \quad (24)$$

$$D_u^B \approx 1.04(1 + 5.4u)^{0.5} \quad (25)$$

$$r_{rs}^{dp} \approx (0.084 + 0.170u)u \quad (26)$$

Where D_u^C and D_u^B are the optical path elongation factors for scattered photons for the water column and bottom respectively. r_{rs}^{dp} is the underwater remote sensing reflectance for optically deep water, k is the total attenuation coefficient and H is the average bottom depth of the water. Average H values of 1.5, 2.1, 3.5, and 1 m were used for Binnenschelde, Markiezaatsmeer and Kristalbad respectively. Θ and Θ_w are the subsurface viewing angle (30^0) and subsurface solar zenith angle (in radians) respectively. The bottom albedo (ρ) of each lake at each site was then computed from eq. (23).

Also, $r_{rs} \approx (r_{rs}^C) + (r_{rs}^B)$, sum of the contribution of the underwater reflectance of the water column (r_{rs}^C) and the underwater reflectance from the bottom of the water (r_{rs}^B) (Lee et al., 1999). Therefore, (r_{rs}^C) and (r_{rs}^B) were calculated using eq. (27) and (28) respectively.

$$r_{rs}^C = r_{rs}^{dp}\left(1 - \exp\left\{-\left[\frac{1}{\cos\theta_w} + \frac{D_u^C}{\cos\theta}\right]\kappa H\right\}\right) \quad (27)$$

$$r_{rs}^B = \frac{1}{\pi}\rho \exp\left\{-\left[\frac{1}{\cos\theta_w} + \frac{D_u^B}{\cos\theta}\right]\kappa H\right\} \quad (28)$$

4.10. Computing Euphotic Depth from In-situ measurements

The spectral range (400-700) nm is usually used by photosynthetic organisms for the process of photosynthesis (Lee et al., 2005). This spectral range is known as Photosynthetically Active radiation (PAR). According to Mobley (2004), the depth of penetration of the solar radiation where PAR is reduced to 1% of the initial value at the surface is known as euphotic depth (Z_{eu}). In this study, euphotic depth zone was derived directly from the attenuation coefficient of the photosynthetically active radiation (K_d(PAR)). This was done by first computing the underwater irradiance at different depths for the visible range (400-700 nm) as shown in eq. (29). The Euphotic depth zone for each site was then computed directly from the in-situ derived K_d(PAR) by applying eq. (30).

$$PAR(z) = \int_{400}^{700} E_d\,(\lambda; z)\,d\lambda \quad (29)$$

$$Z_{eu} = \frac{4.605}{K_d(PAR)} \quad (30)$$

5. RESULTS AND DISCUSSION

This chapter presents the details of results and discussion of the major findings in this research. These are the spectral signatures of the lakes, diffuse attenuation coefficients, spectral signature of SAV, SAV distribution and NDVI of Binnenschelde. Statistics of results of laboratory measurements of water quality indicators are also presented here. Derived bottom albedos as well as the range of euphotic depth range of the inland lakes are also discussed.

5.1. Water leaving reflectance

The respective water leaving reflectances (spectral reflectance signatures) of the four study areas as described in section 4.3. are shown in figure 12. There is variation in water leaving reflectance with wavelength and at different points of measurements for all the lakes. This variation is caused by the absorption and scattering of the incident light at different wavelengths. This indicates the variation of IOPs and hence variation in absorption and scattering with wavelength for different points at the same lake. Variability of Rrs at different points of measurement is however higher in Markiezaatsmeer compared to the other lakes.

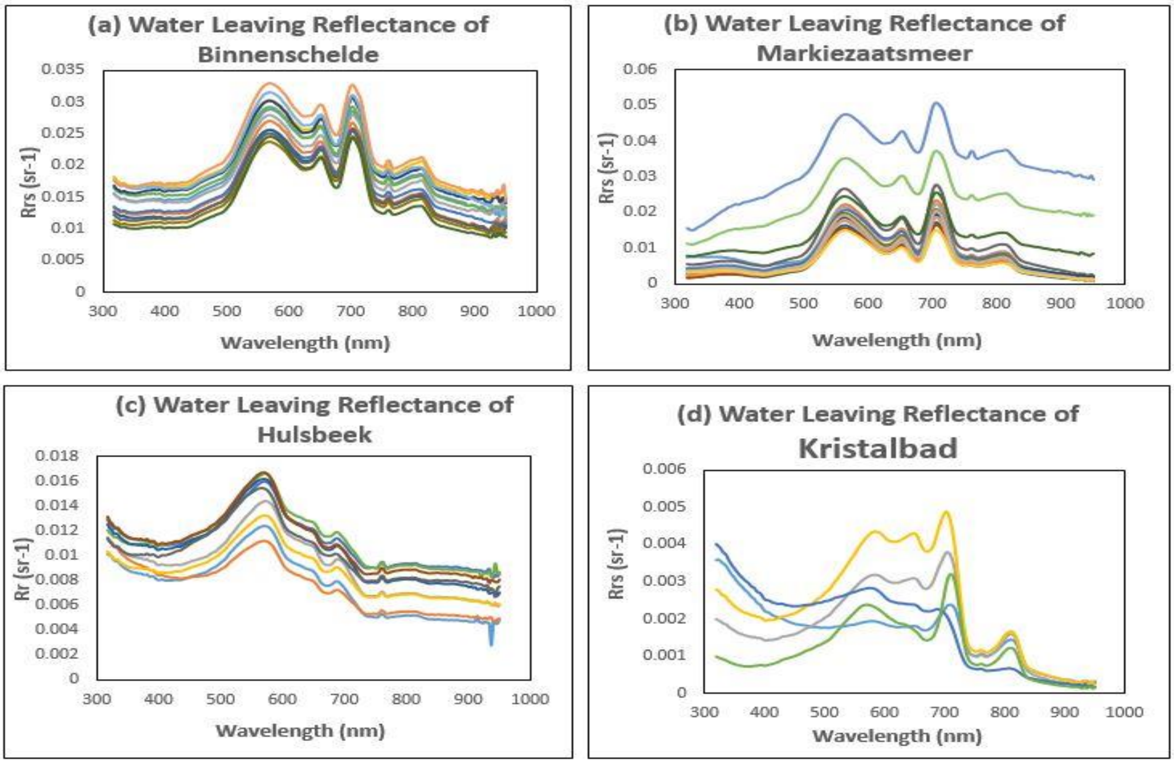

Figure 12. Water leaving reflectance of Binnenschelde, Markiezaatsmeer, Hulsbeek and Kristalbad.

The reflectance is fairly low in the blue spectral range (400-500 nm) for all the lakes. The reflectance starts increasing from 500 nm and peaks at about 560 nm. There is also a peak at around 705 nm, associated to the absorption and scattering by water and phytoplankton (Gitelson et al., 2007; Matthews et al., 2010) which decreases to about 780 nm. It increases again at 820 nm and finally decreases to about 930 nm. This illustrates the characteristics of typical turbid and productive inland waters (Gitelson et al., 2007). These variations in Rrs are highly significant as it provides information regarding the optical properties of different constituents present in the water (Salama et al., 2009).

5.2. Diffuse attenuation coefficients

Figure 13 illustrates that there is an inverse relation between Rrs(λ) and Kd (λ) (computed at 0.1 and 0.2 m depth). It can clearly be seen that a trough from 400-500 nm wavelength in the Rrs (figure 12) produces a peak in the same wave length range in K_d (figure 13). Similarly, a peak of Rrs from 500-560 nm produces a trough in K_d for the same wave length range. The attenuation at about 700 nm or reflectance peak at same wavelength indicates the high concentration of phytoplankton (Gitelson et al., 2007; Matthews et al., 2010). This is especially so for Binnenschelde and Markiezaatsmeer.

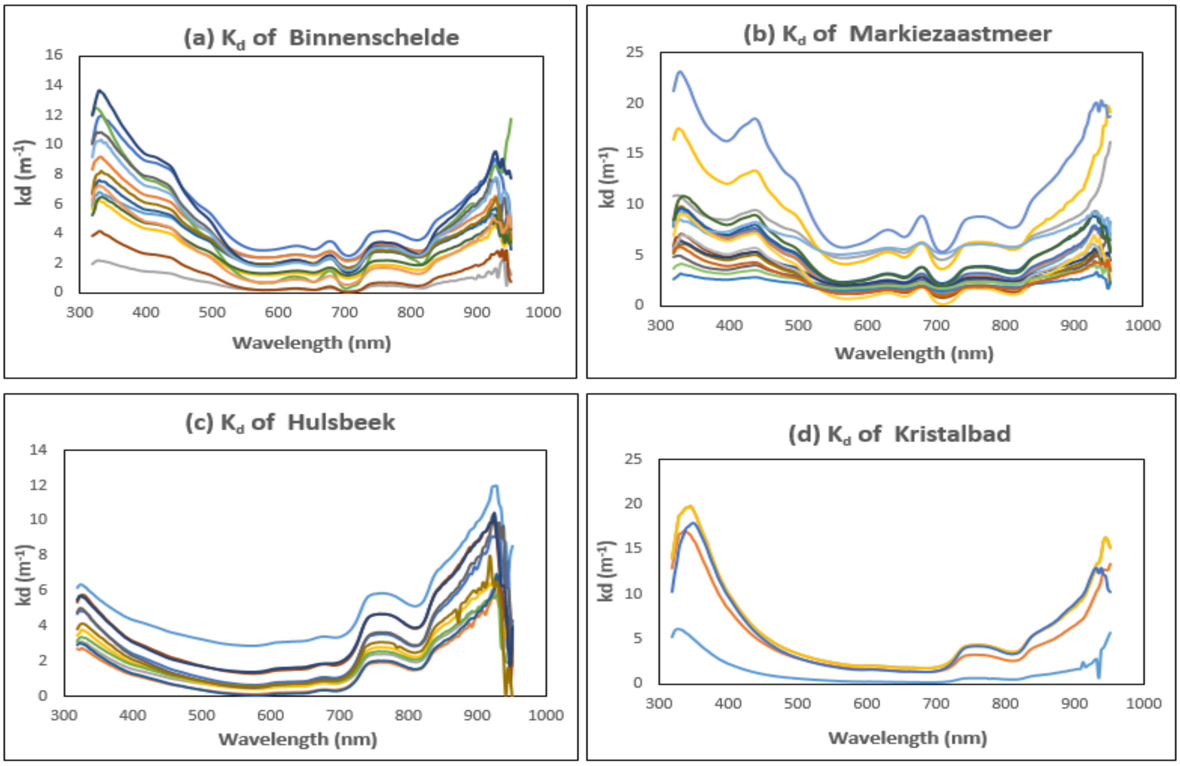

Figure 13. Diffuse attenuation coefficient of Binnenschelde (a), Markiezaatsmeer (b), Hulsbeek (c) and Kristalbad (d) derived from in-situ measurement.

5.3. Spectral Signature of SAV in the Binnenschelde lake

Using spectral features of SAV, different SAV species can be discriminated at some particular wavelengths (David et al., 2003). The focus of this study however is not on the discrimination of different SAV species. The in-situ measured spectral reflectance signature of SAV in the Binnenschelde is presented in figure 14. The wavelength range (a) 540-560 nm indicates the reflectance of green by plants which accounts for the green colour of plants the human eye perceives (Knipling, 1970). Also, (b) 670-690 nm is the red absorption range by chlorophyll, (c) 710-730 nm represents the first reflectance peak in the NIR, (d) 735-745 nm shows the dip in NIR and (e) 810-820 nm indicates the second dip in the NIR band (Cho et al., 2008).

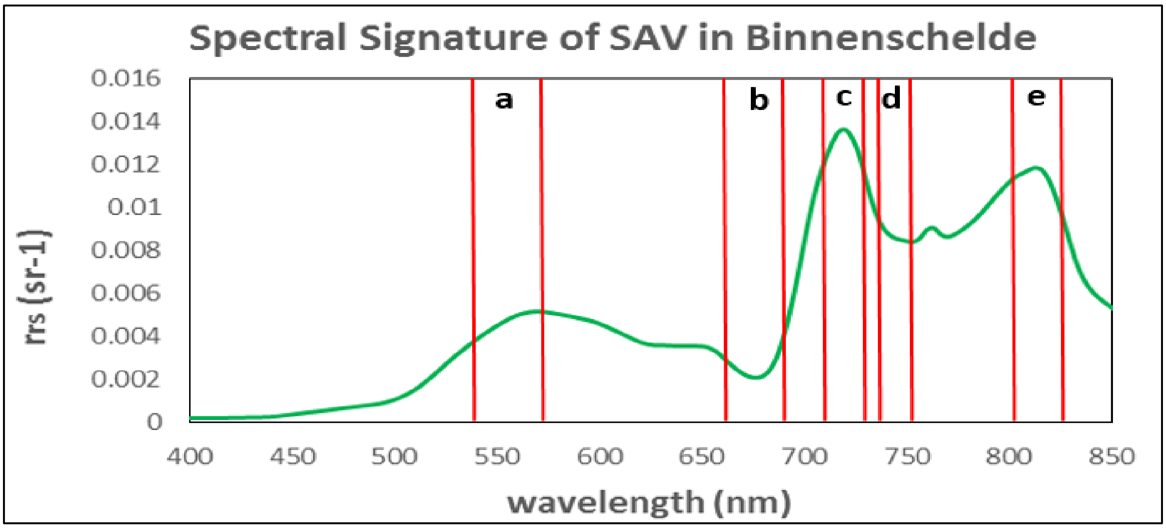

Figure 14. Spectral signature of SAV in Binnenschelde showing unique wavelength ranges of SAV reflectance measured under water.

Unlike water (without SAV), SAV has a very high intensity of absorption in the blue wavelength (400-500 nm) and around the red (675 nm) (Yuan & Zhang, 2008). Therefore, SAV can be identified by an increased absorption at the blue band and increased reflectance at the green band (Cho, 2007). With reference to the above spectral characteristics of SAV, field end members were selected and a spectral library of SAV built for the SAM classification.

5.3.1. Spectral Signature of SAV and high concentration of chlorophyll a

From the laboratory analysis, the highest concentration of chlorophyll a in Binnenschelde is 7.141 mg/m^3. Though discrimination of high concentration of chlorophyll a and SAV is not the aim of this study, from figure 15, it can be seen that there are spectral similarities between high concentration of chlorophyll a and SAV. There are reflectance peaks around 540 nm to 560 nm (green) in both signatures. Also, they both have absorption troughs around 670nm to 690nm (red) wavelength. Separation of high concentration of chlorophyll a, algal bloom and SAV is very difficult because these similarities (Malthus et., 1997). However, some unique differences can be observed between them. For the high concentration of chlorophyll a signature, there is higher reflectance in the visible wavelength range and lower reflectance peak in the NIR than that of the SAV signature. Similar trend was reported by Gin et al., (2002) for water with high concentration of chlorophyll a.

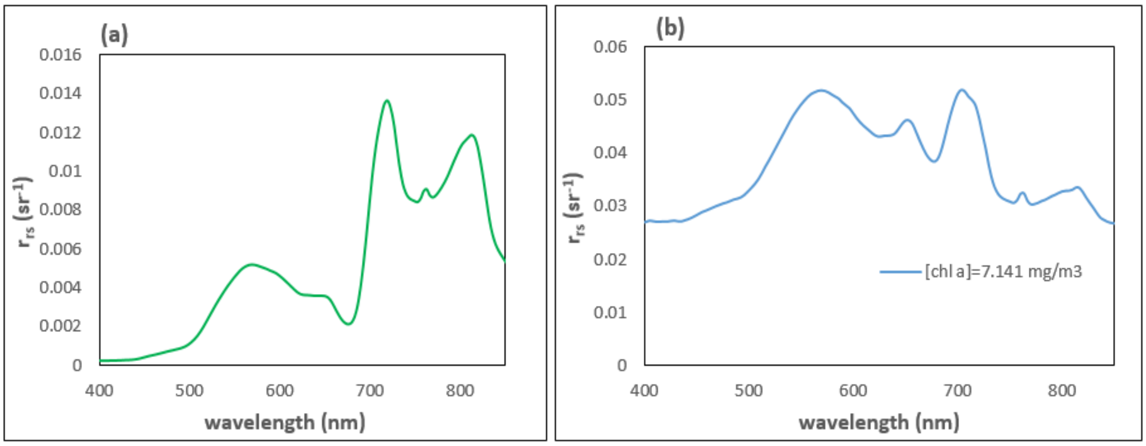

Figure 15. Plots showing the spectral signatures of SAV (a) and high concentration of chlorophyll a (b) in the Binnenschelde (just below the surface of the water).

5.4. Distribution and Spatiotemporal Variation of SAV in Binnenschelde

The distribution and spatial variation of SAV with time using the remote sensing reflectance of SAV and water only classes is presented here. Classification of SAV was done using the atmospherically corrected images of Landsat 8 OLI and Spot 6 MS sensors. SAV growing season starts around April to October each year (Oyama, 1993; Court et al.,1993). The interaction of several environmental factors influences the growth, distribution, production and species composition of SAV (Barko & Smart, 1986). The depth and turbidity of the overlying water column greatly affect the accurate detection of SAV (Hunter et al., 2010). Growth of SAV is also affected by the supply of light and epiphytic biofilms (Köhler et al., 2010). Since the temporal variation SAV is much lower than that of the water, the ability of a remote sensor to 'see' SAV will depend on the IOPs of the water such us low turbidity (high clarity). For this reason, the approach we used in this study was to sum the classified images. Weights were then assigned to SAV pixels in the classified images as indicated in table 5. The classified Landsat 8 images were then summed and reclassified based on the weights assigned. The resultant image therefore shows the probability of finding SAV from April, 2015 to September, 2015 (see figure 17).

Table 5. Probability of occurrence and weights assigned to SAV pixels in the Binnenschelde.

Probability of Occurrence (SAV pixels)	Assigned Weight
¼	25%
2/4	50%
¾	75%
4/4	100%

From figure 16, it can be seen that a greater area of the lake was classified as water (blue or 0%) and the highest probability of SAV occurrence is 75%. This is practically not true since the temporal variability of SAV is very low compared to the water. It however means that some pixels of SAV have been classified as water and vice versa due to the temporal variability of the IOPs of water as mentioned earlier. Since we have only a single day of turbidity measurement, we cannot conclusively state which image was misclassified.

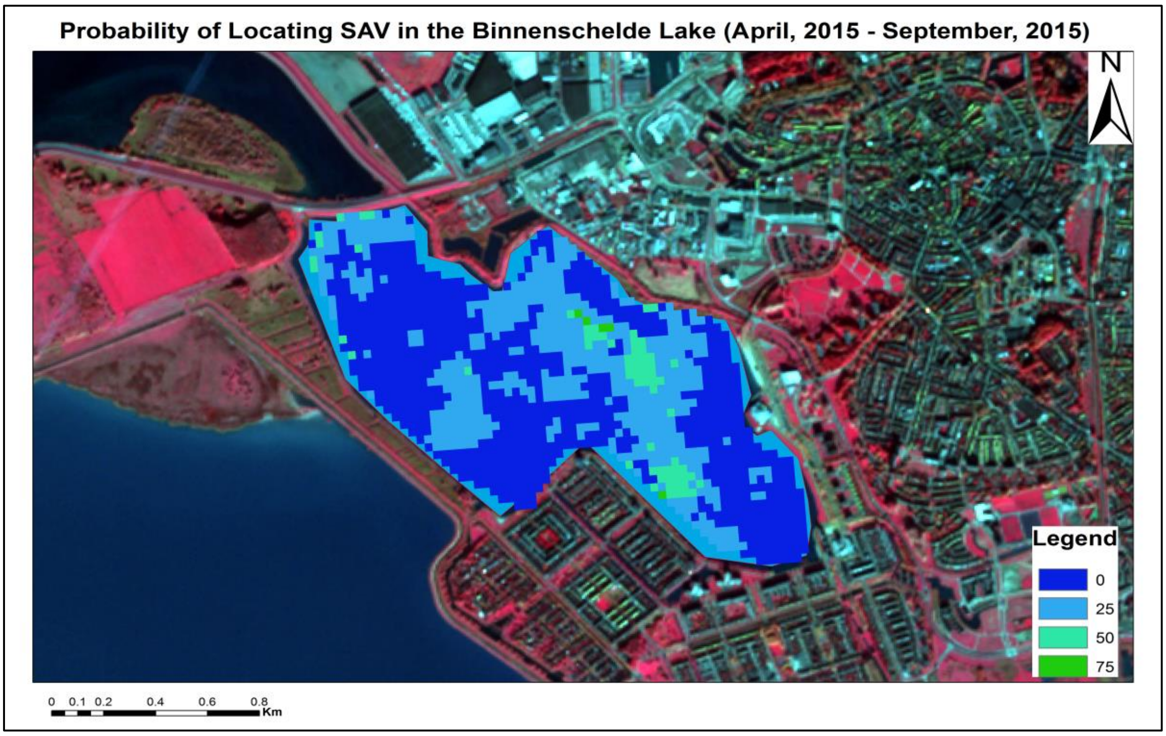

Figure 16. SAV distribution map of Binnenschelde (20/04/15, 07/06/15, 03/08/15 and 27/09/15 classified images) overlaid on a SPOT 6 image. Classified images were summed and weights assigned to SAV pixels based on the number of images they appeared.

5.4.1. Accuracy Assessment of SAM classification

Confusion matrix, a post classification tool in ENVI was used to assess the accuracy of the SAM classification. Ground truth regions of interest (ROI) were used to do the assessment. Only the 27/09/15 (Landsat 8) classified image was assessed because field measurement was done on 24/09/15 and ground truth of the classes are known. Report of the accuracy assessment is presented in table 6. There was an overall accuracy of 89.535 % in the classification of the 27/09/15 Landsat 8 image of Binnenschelde and a user accuracy values of 96% and 86.89% for SAV and water respectively. This shows a very good classification of the SAV and water, especially the SAV class. This is attributed to the accurate knowledge of the SAV location based on field observation.

Table 6. Report of accuracy assessment of 27/11/15 Landsat 8 image classification (Binnenschelde).

Overall Accuracy = (77/86) 89.53%
Kappa Coefficient = 0.7656

	Ground Truth (Pixels)		
Class	SAV_aa	water_aa	Total
Unclassified	0	0	0
SAV :C2	24	1	25
water [Blue]	8	53	61
Total	32	54	86

	Ground Truth (Percent)		
Class	SAV_aa	water_aa	Total
Unclassified	0.00	0.00	0.00
SAV :C2	75.00	1.85	29.07
water [Blue]	25.00	98.15	70.93
Total	100.00	100.00	100.00

Class	Commission (Percent)	Omission (Percent)	Commission (Pixels)	Omission (Pixels)
SAV :C2	4.00	25.00	1/25	8/32
water [Blue]	13.11	1.85	8/61	1/54

Class	Prod. Acc. (Percent)	User Acc. (Percent)	Prod. Acc. (Pixels)	User Acc. (Pixels)
SAV :C2	75.00	96.00	24/32	24/25
water [Blue]	98.15	86.89	53/54	53/61

5.4.2. Linear Unmixing of water and SAV pixels

Spectral linear unmixing was applied to the 27/09/15 Landsat 8 image because of our ground truth knowledge of SAV points. The spectral unmixing of the Landsat 8 image of Binnenschelde produced three sub-images in three bands. Band 1 is the map showing the spectrally unmixed water pixels, band 2 map of spectrally unmixed SAV pixels and band 3 is the root mean square (RMS) error map of the unmixing process. The RMS error map shows the level of error (the uncertainty) in the mixing calculations. These maps are shown in figures 17, 18 and 19. It can be seen that areas with high fractions of SAV (figure 17) have very low corresponding fractions of water (figure 18) and vice versa. With regards to the uncertainty in the unmixing calculations (figure 19), it can be seen that there is high error at the edges of the image.

This is because of the above water aquatic vegetation found at the edges of the lake. The above water vegetation end members were not included in the unmixing end members and hence high error in the unmixing process into fractions of SAV and water.

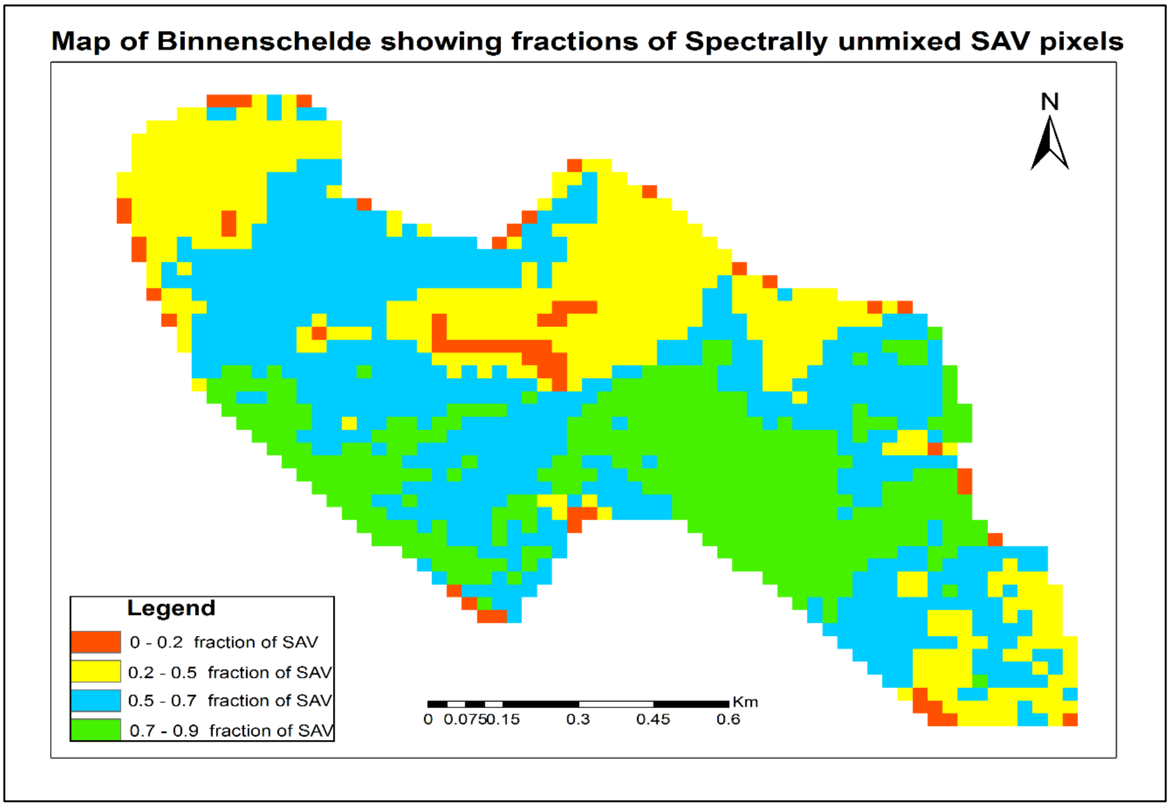

Figure 17. Map showing the fractions of spectrally unmixed pixels of SAV in the unmixing process (Landsat 8, 27/09/15).

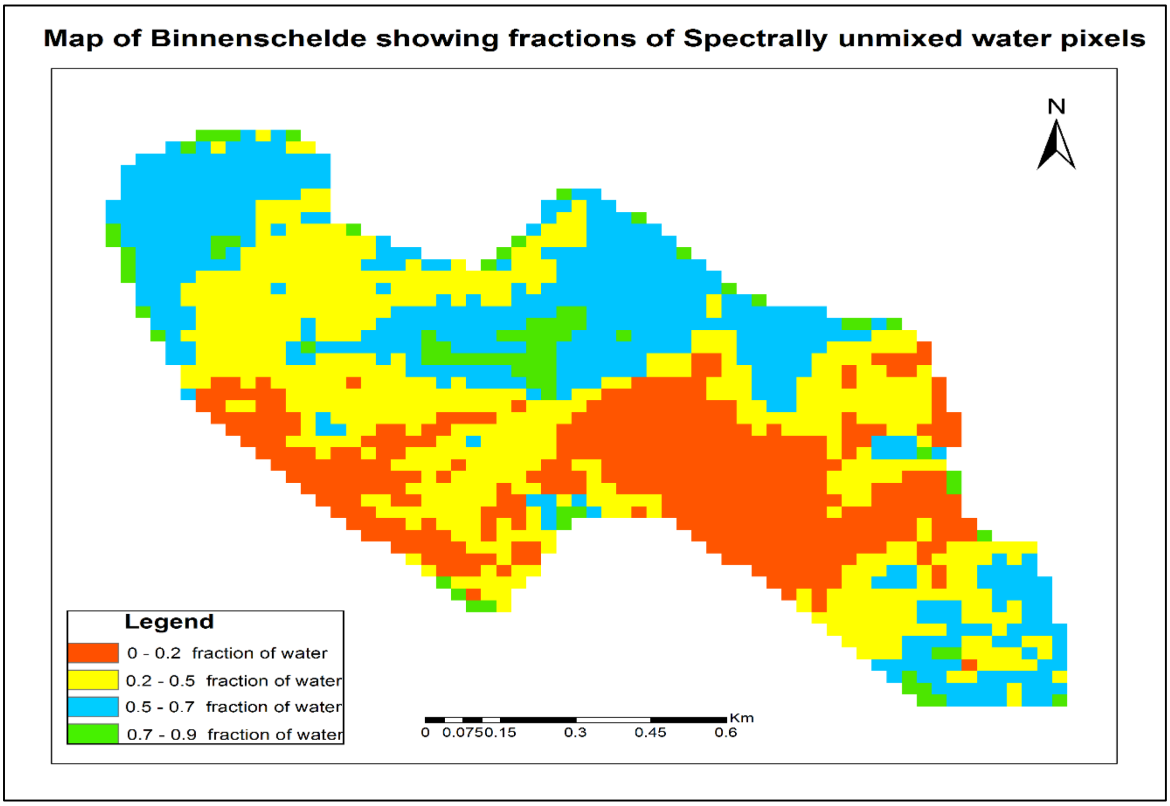

Figure 18. Map showing the fractions of spectrally unmixed pixels of water in the unmixing process (Landsat 8, 27/09/15).

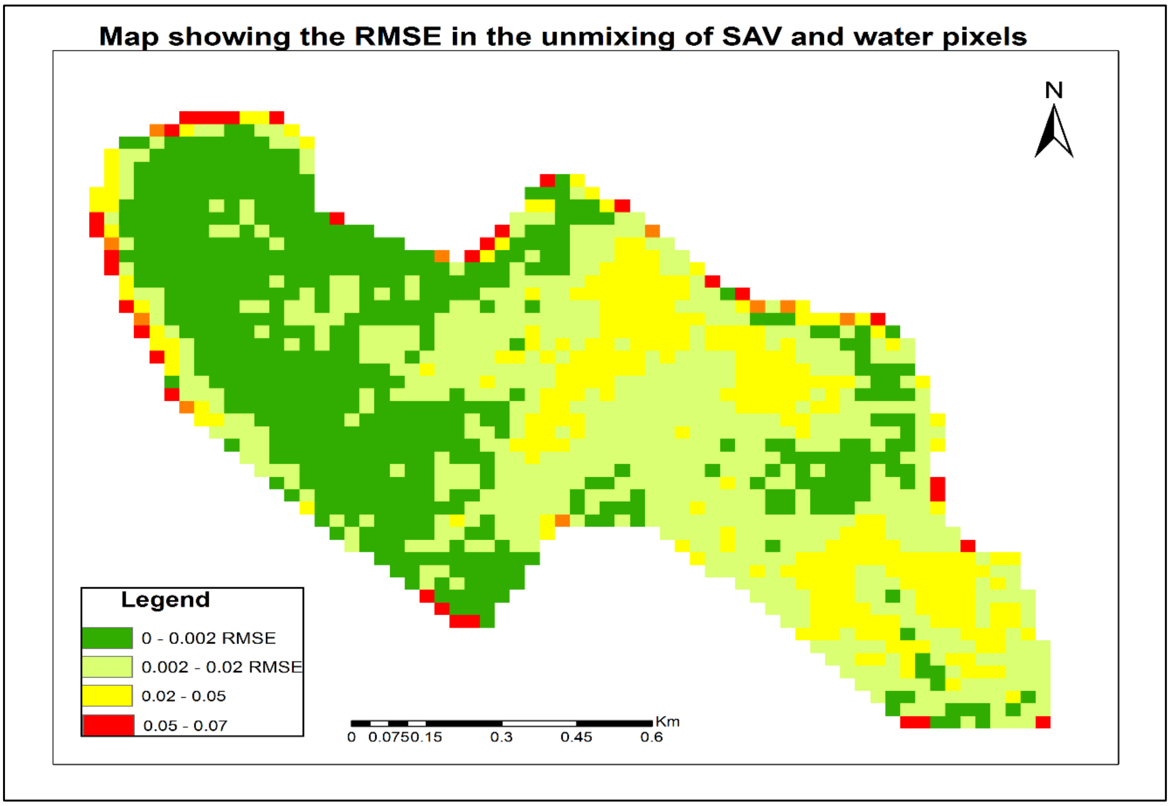

Figure 19. Map showing the RMSE (uncertainty) of the spectral unmixing process of SAV and water pixels (Landsat 8, 27/09/15).

5.5. NDVI as Indicator of SAV Abundance

NDVI maps were created to serve as indicators of the presence of SAV using the reflectance satellite images obtained after the atmospheric correction. The distinctive high reflectance values of green plants in the NIR band and low reflectance in the visible band (Hyun Jung Cho & Lu, 2010) were used to obtain different NDVI classes. Threshold values were set in order to discriminate areas of water, SAV and above water vegetation as shown in table 7. Negative values represent the absence of vegetation or the lake bottom (Liira et al., 2010). Plants covered with water levels of 20 – 25 cm have NDVI values of about 0.15 (Beget & Di Bella, 2007). High positive NDVI values (greater than 0.15) were assigned to above water vegetation which also increase with density of the vegetation (Holben, 1986). In this study, SAV was evident in areas with NDVI from 0 to 0.15.

Table 7. Thresholds set and wavelengths used to calculate NDVI.

Index	**Class Assigned**	**Wavelengths (μm)** (a) Landsat 8 (b) SPOT 6	**Threshold Values**
	Water		NDVI < 0
NDVI	SAV	(a) (0.865-0.655)/ (0.865+0.655)	0 < NDVI < 0.15
	Above water vegetation	(b) (0.825-0.660)/ (0.825+0.660)	NDVI > 0.15

The results obtained are shown in appendix 1. From the results the following observations were made:

1. NDVI maps showed some similarities with pattern of the classified SAV maps. There was generally high NDVI and hence high density of SAV in both 20th April and 7th June Landsat 8 images in the western part of Binnenschelde. However, the 3th August NDVI map showed some patches of SAV in the middle and south eastern part of the Binneschelde Lake. This shift in density in just three months could largely be due to the temporal variation of IOPs of the water caused by change in turbidity.
2. Areas with NDVI values greater than 0.15 were observed at the edges of the lake. These areas are known (from field observation) to contain above water aquatic vegetation but not SAV.
3. All the NDVI maps of both Landsat 8 and Spot 6 showed areas of above water vegetation for all the different days at the edges of the lake.
4. Even though there were still traces of SAV in November and December, 2015 NDVI maps, they could only be seen at the edges of the lakes as shown in the SPOT 6 NDVI images. This indicates the unavailability of SAV after the end of the growing season in October.

5.6. Water Quality Indicators

Statistics of results (minimum, mean, maximum and standard deviation) of the laboratory analysis as described in section 3.2 are presented in table 8. SPM concentration ranges from 58-70 mg/l (Binnenschelde), 92-136 mg/l (Markiezaatsmeer), 7.5-27.5 mg/l (Hulsbeek) and 6-22 mg/l (Kristalbad). The range of Rrs values for 400-900 nm range are 0.0093-0.0330 sr^{-1}, 0.0016-0.0509 sr^{-1}, 0.0028-0.01670, and 0.0001-0.0049 sr^{-1} for Binnenschelde, Markiezaatsmeer, Hulsbeek and Kristalbad respectively. This pattern shows that the concentration of SPM increased with Rrs as reported by Doxaran et al., (2003). Also, the variability of the reflectance spectra (see figure 12) at different points and at different lakes is supported by the variation in the results of the laboratory measurements of the water samples taken at those points (Zhongping Lee & Carder, 2004).

Table 8. Statistics of laboratory measured water quality variables of all the lakes.

Statistics	**SPM** (mg/l)	**Turbidity** (NTU)	**C-DOM** absorption at 440 nm	**chlorophyll a** conc. (mg/m^3)
Minimum	6	1.396	0.006	3.621
Mean	49.182	11.183	0.957	9.422
Maximum	136	27.640	3.729	25.703
Std	42.746	10.410	1.053	5.397

5.7. Spectrum of Derived Bottom Albedos

In-situ derived bottom albedos of selected sites are presented in figure 20. Even though Binnenschelde and Markiezaatsmeer have similar bottom albedo spectrums, the bottom albedos of Markiezaatsmeer are generally higher. Each lake has a spectrally distinct bottom albedo even at each site. In shallow waters, bottom reflectance greatly affects the remotely sensed signal (Ma et al., 2011) just as different constituents present in the water (Albert & Gege, 2006). The low bottom albedo values observed below the 500 nm wavelength and around 675 nm are associated with the presence of chlorophyll a at those sites (Maritorena et al., 1994). The sharp increase in the albedo value at 675 nm (Binnenschelde) is an indication of a vegetated bottom (Ma et al., 2011).

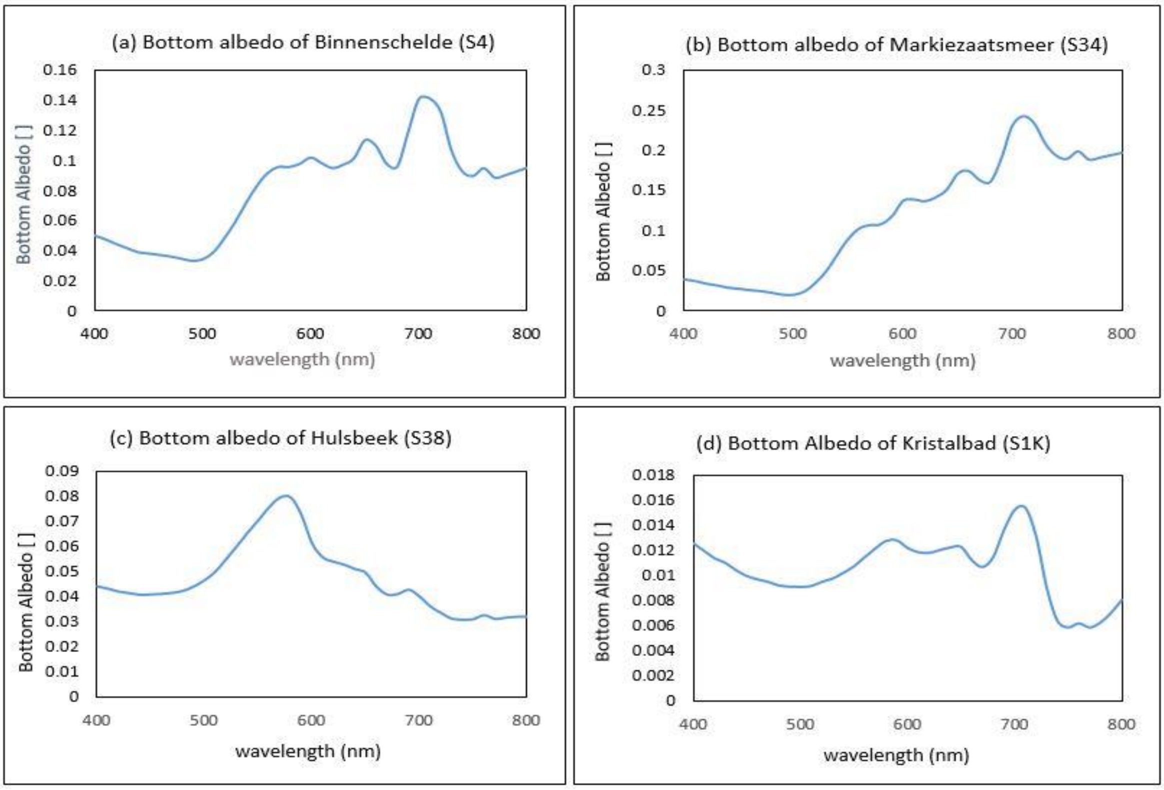

Figure 20. Selected site bottom albedos of Binnenschelde (a), Markiezaatsmeer (b), Hulsbeek (c) and Kristalbad (d).

5.8. Variability and Standard deviation of r_{rs}

Figure 21 shows the variability of the sub-surface remote sensing reflectance (r_{rs}) derived from in-situ measurements. For each lake, the error bars (black vertical lines) indicate the standard deviation of derived r_{rs} from their mean values with respect to wavelength. Variability of underwater remote sensing reflectance is generally uniform in all wavelengths but higher in Markiezaatsmeer compared to the other lakes. The r_{rs} signal is influenced by the reflectance of the water column and bottom (Lee et al., 1999). Therefore the variability of r_{rs} is caused by the variation in reflectance of the water column and bottom at each point of each lake.

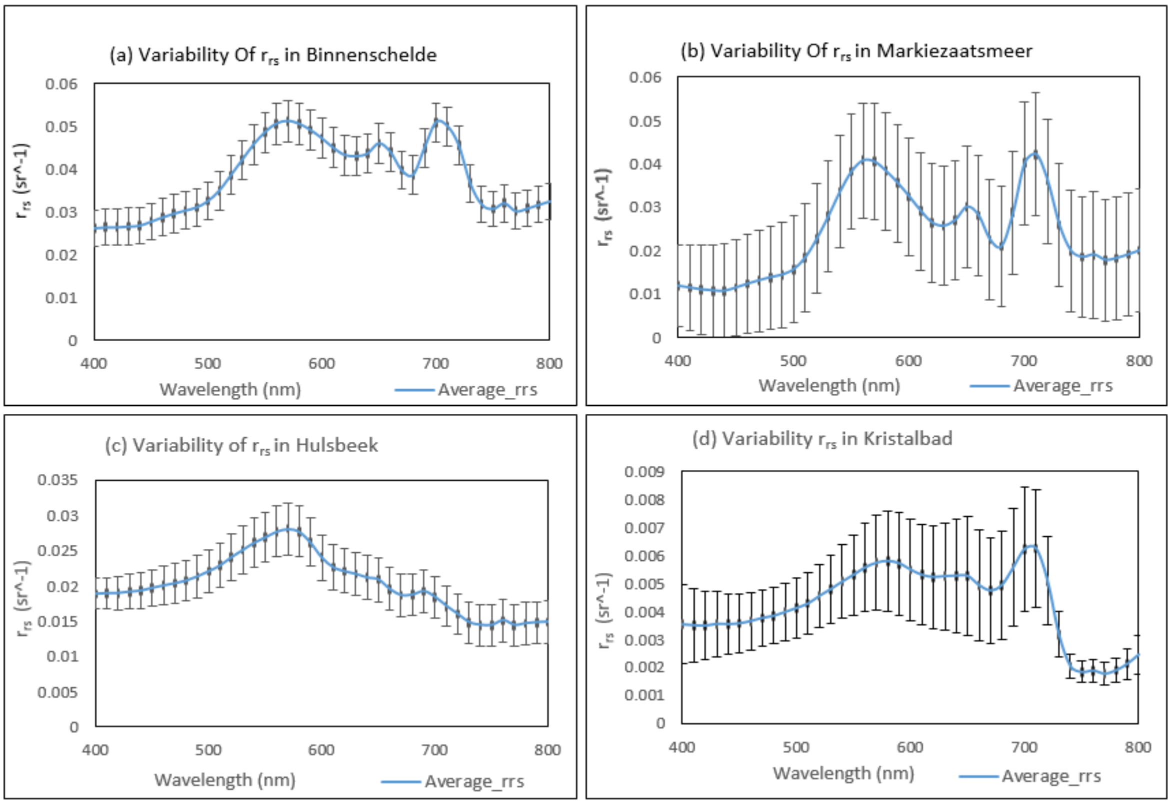

Figure 21. Standard deviation and variability of remote sensing reflectance evaluated just below the surface of the water (r_{rs}) for Binnenschelde (a), Markiezaatsmeer (b), Hulsbeek (c) and Kristalbad (d).

5.9. Euphotic Depth of the inland Lakes

Though the average depth of Binnenschelde and Markiezaatsmeer are 1.5 m and 2.1 m respectively, Binnenschelde has a higher range of euphotic depth (see table 9). This means that there is higher light penetration in the Binnenschelde than in the Markiezaatsmeer. The clarity of Hulsbeek was so high that the bottom of the deepest point (about 6 m) could be seen with an unaided eye (which is within the visible range (400-700) nm). This has also been confirmed by its high values of euphotic depth computed. The value of Z_{eu} is a highly significant water quality indicator of an ecosystem and determines the primary production in the water column (Zhongping Lee et al., 2007). The range of the in-situ derive euphotic depths concur with previous study of optically shallow in land waters (Majozi et al., 2014) aside Hulsbeek which has uniquely high clarity and hence high Z_{eu}..

Table 9. Range of K_d (PAR) and Z_{eu}.

Study Area	Range of K_d (PAR) [m-1]	Range of Z_{eu} [m]
Binnenschelde	1.57 - 3.98	1.16 - 2.93
Markiezaatsmeer	1.78 - 8.67	0.53 - 2.59
Hulsbeek	0.75 - 3.24	1.42 - 6.12
Kristalbad	2.57 - 3.04	1.51 - 1.79

6. CONCLUSION AND RECOMMENDATION

6.1. Conclusion

The main aim of this study was to delineate and quantify submerged aquatic vegetation (SAV), analyse their spatiotemporal variability using multi-spectral sensors in the Binnenschelde and Markiezaatsmeer lakes in the Netherlands. Based on the results obtained in the study, the following conclusions were therefore made;

- The classification of SAV was based on the field measured spectral signature of SAV. Results of the SAV classification indicate that IOPs of inland lakes highly influence the detection and classification of SAV. This is even more important because of the similarity in the spectral signature of SAV and high concentration of chlorophyll a.
- The spatiotemporal variation of SAV cannot be accurately monitored without adequate knowledge of their spatial extent (ground truth) at high temporal resolution.
- The highest Z_{eu} was at the Hulsbeek Lake. This accurately confirmed the field observation made since the bottom of deepest point of that lake could even be seen with our unaided eyes.
- Bottom albedos (ρ), underwater remote sensing reflectance contribution of the water column (r_{rs}^{C}) and bottom (r_{rs}^{B}) derived from the in-situ measurement confirm the contribution of bottom reflectance in optically shallow lakes. This result would help in the development of models for optically shallow waters in the future.

6.2. Recommendations

Several factors affected the results of this research. Some of these factors could be avoided or minimised but others may not. On this basis, I make the following recommendations.

- Results obtained only represent the IOPs of the lakes for the period of sampling. There is the need for more measurements to be carried out in future for better understanding of the IOPs of all the lakes as one day of field measurement is not enough to draw a reasonable conclusion on both their spatial and temporal variations.
- There is the need for finer temporal and spatial resolution satellite images in mapping SAV in the future to provide better detail on SAV distribution. More ground truth SAV measurements should be done for more accurate assessment of SAV classification.
- Due to limited access to the Kristalbad wetland, sample points taken were inadequate. Future study therefore should take more representative measurements.

- It is highly challenging to obtain cloud free images. Future study should consider acquiring more images for better analysis of the delineation of SAV.

LIST OF REFERENCES

Abbenhues, C. (Province of O. (2003). *Provinciale Staten van Overijssel Postbus 10078 8000 GB ZWOLLE*. Zwolle. Retrieved from www.prv-overijssel.nl (5th January,2016).

Akkaynak, D., Allen, J. J., Mäthger, L. M., Chiao, C. C., & Hanlon, R. T. (2013). Quantification of cuttlefish (Sepia officinalis) camouflage: A study of color and luminance using in situ spectrometry. *Journal of Comparative Physiology A: Neuroethology, Sensory, Neural, and Behavioral Physiology*, *199*(3), 211–225. http://doi.org/10.1007/s00359-012-0785-3

Albert, A., & Gege, P. (2006). Inversion of irradiance and remote sensing reflectance in shallow water between 400 and 800 nm for calculations of water and bottom properties. *APPLIED OPTICS*, *45*(10), 2331–2343. http://doi.org/10.1364/AO.45.002331

Azzella, M. M., Rosati, L., Iberite, M., Bolpagni, R., & Blasi, C. (2013). Changes in aquatic plants in the Italian volcanic-lake system detected using current data and historical records. *Aquatic Botany*, *112*, 41–47. http://doi.org/10.1016/j.aquabot.2013.07.005

Barko, J. W., & Smart, R. M. (1986). Sediment-Related Mechanisms of Growth Limitation in Submerged Macrophytes. *Ecological Society of America*, *67*(5), 1328–1340. http://doi.org/10.2307/1938689

Beget, M. E., & Di Bella, C. M. (2007). Flooding: The effect of water depth on the spectral response of grass canopies. *Journal of Hydrology*, *335*(3-4), 285–294. http://doi.org/10.1016/j.jhydrol.2006.11.018

Bernstein, L. S., Adler-Golden, S. M., Sundberg, R. L., Levine, R. Y., Perkins, T. C., Berk, A., … Hoke, M. L. (2005a). A new method for atmospheric correction and aerosol optical property retrieval for VIS-SWIR multi- and hyperspectral imaging sensors: QUAC (QUick Atmospheric Correction). In S. S. I. B. MA (Ed.), *International Geoscience and Remote Sensing Symposium (IGARSS)* (Vol. 5, pp. 3549–3552). http://doi.org/10.1109/IGARSS.2005.1526613

Bernstein, L. S., Adler-Golden, S. M., Sundberg, R. L., Levine, R. Y., Perkins, T. C., Berk, A., … Hoke, M. L. (2005b). Validation of the QUick Atmospheric Correction (QUAC) Algorithm for VNIR-SWIR Multi- and Hyperspectral Imagery. *International Society for Optics and Photonics*, 668–678. http://doi.org/10.1117/12.603359

Boardam J. W., Kruse, F. A. (1994). Automated spectral analysis: a geologic example using AVIRIS data, north Grapevine mountains, Nevada. In *Tenth Thematic Conference on Geological Remote Sesnsing, 9-12 May 1994* (pp. I–407 – I–418). San Antonio, Texas.

Boardman, J. W. (1989). Inversion Of Imaging Spectrometry Data Using Singular Value Decomposition. In *Geoscience and Remote Sensing Symposium, 1989. IGARSS'89.* (Vol. 4, pp. 2069–2072). New York. http://doi.org/10.1109/IGARSS.1989.577779

Carder, K. L., Steward, R. G., Harvey, G. R., & Ortner, P. B. (1989). Marine humic and fulvic acids: Their effects on remote sensing of ocean chlorophyll. *Limnology and Oceanography*, *34*(1), 68–81. http://doi.org/10.4319/lo.1989.34.1.0068

Carder, K. L., Hawes, S. K., Baker, K. A., Smith, R., Steward, R. G., & Mitchell, B. G. (1991). Reflectance model for quantifying chlorophyll a in the presence oi productivity degradation products. *Journal of Geophysical Research*, *96*(C11), 20599–20611. http://doi.org/10.1029/91JC02117

Cho, H. J. (2007). Depth - variant spectral characteristics of submersed aquatic vegetation detected by Landsat 7 ETM +. *International Journal of Remote Sensing*, *28*(7), 1455–1467. http://doi.org/10.1080/01431160600962772

Cho, H. J., & Lu, D. (2010). A water-depth correction algorithm for submerged vegetation spectra. *Tailor and Francis. Remote Sensing Letters*, *1*(1), 29–35. http://doi.org/10.1080/01431160903246709

Cho, H. J., Lu, D., Kelley, J., Mcgregor, L., & Sciences, A. (2008). Experimental Approach to Improve Canopy Area Estimation of Submerged Vegetation. In *Proceedings of 2008 International ESRI User Conference. Water Correction Algorithm Application for Underwater Vegetation Signal Improvement. Cho, Lu* (pp. 1–11). Washington.

Court Stevenson, Lorie W. Staver, K. W. S. (1993). Water quality associated with survival of submersed aquatic vegetation along an estuarine gradient. *Estuaries*, *16*(2), 346–361. http://doi.org/10.2307/1352507

Curtarelli, M. P., Ogashawara, I., Alcantara, E. H., Lorenzzetti, J. A., & Stech, J. L. (2014). Spatial and temporal dynamic of the trophic state in a large amazonian hydroelectric resevoir. In *July, 2014 IEEE International Geoscience and Remote Sensing Symposium (IGARSS)* (pp. 890 – 893). IEE. http://doi.org/10.1109/IGARSS.2014.6946568

David J. Williams, N. B. R., Lombana, A. V., & Gomez4, T. M. O. A. R. B. (2003). Preliminary Investigation of Submerged Aquatic Vegetation Mapping using Hyperspectral Remote Sensing. *Environmental Monitoring and Assessment*, *81*(1-3), 383–392. http://doi.org/10.1023/A:1021318217654

Diaz, R. J., Solan, M., & Valente, R. M. (2004). A review of approaches for classifying benthic habitats and evaluating habitat quality. *Journal of Environmental Management*, *73*(3), 165–181. http://doi.org/10.1016/j.jenvman.2004.06.004

Dobigeon, Nicolas Dobigeon, N., Tourneret, J. Y., & Chang, C. I. (2008). Semi-Supervised Linear Spectral Unmixing Using a Hierarchical Bayesian Model for Hyperspectral Imagery. *IEEE Transactions on Signal Processing*, *56*(7), 2684–2695. http://doi.org/10.1109/TSP.2008.917851

Doxaran, D., Froidefond, J., & Castaing, P. (2003). Remote-sensing reflectance of turbid sediment-dominated waters . Reduction of sediment type variations and changing illumination conditions effects by use of reflectance ratios. *Applied Optics*, *42*(15), 2623–2634. http://doi.org/10.1364/AO.42.002623

Flynn, K., & Chapra, S. (2014). Remote Sensing of Submerged Aquatic Vegetation in a Shallow Non-Turbid River Using an Unmanned Aerial Vehicle. *Remote Sensing*, *6*(12), 12815–12836. http://doi.org/10.3390/rs61212815

Giesen, W., Vankatwijk, M. M., & Denhartog, C. (1990). Eelgras condition and turbidity in the Dutch Wadden Sea. *Aquatic Botany*, *37*(1), 71–85. http://doi.org/10.1016/0304-3770(90)90065-S

Gilvear, D., Hunter, P., & Higgins, T. (2007). An experimental approach to the measurement of the effects of water depth and substrate on optical and near infra- red reflectance: a field- based assessment of the feasibility of mapping submerged instream habitat. *International Journal of Remote Sensing*, *28*(10), 2241–2256. http://doi.org/10.1080/01431160600976079

Gin, K. Y. H., Koh, S. T., Lin, I. I., & Chan, E. S. (2002). Application of spectral signatures and colour ratios to estimate chlorophyll in Singapore's coastal waters. *Estuarine Coastal and Shelf Science*, *55*(5), 719–728. http://doi.org/10.1006/ecss.2001.0926

Gitelson, A. A., Schalles, J. F., & Hladik, C. M. (2007). Remote chlorophyll-a retrieval in turbid, productive estuaries: Chesapeake Bay case study. *Remote Sensing of Environment*, *109*(4), 464–472. http://doi.org/10.1016/j.rse.2007.01.016

Guide, E. U. S. (2009). Atmospheric correction module: QUAC and FLAASH user's guide, *version*(4), 1–44. Retrieved from http://scholar.google.com/scholar?hl=en&btnG=Search&q=intitle:ENVI+Atmospheric+Correction+Module:+QUAC+and+FLAASH+user's+guide#0 (3rd October, 2015)

Gulati, R. D., & Van Donk, E. (2002). Lakes in the Netherlands, their origin, eutrophication and restoration: State-of-the-art review. In *Ecological Restoration of Aquatic and Semi-Aquatic Ecosystems in the Netherlands (NW Europe) Pages* (Vol. 166, pp. 73–106). Springer Netherlands. http://doi.org/10.1023/A:1021092427559

Hartmann, G. M. (1995). *Studies on the absorption and scattering properties of water constituents for analysis of remote sensing data. Thesis at the Department of Geography and hydrology.* Albert-Ludwigs-University of Freiburg.

Hestir, E. L., Khanna, S., Andrew, M. E., Santos, M. J., Viers, J. H., Greenberg, J. A., … Ustin, S. L. (2008). Identification of invasive vegetation using hyperspectral remote sensing in the California Delta ecosystem. *Remote Sensing of Environment*, *112*(11), 4034–4047. http://doi.org/10.1016/j.rse.2008.01.022

Holben, B. N. (1986). Characteristics of maximum-value composite images from temporal AVHRR data. *International Journal of Remote Sensing*, *7*(11), 1417–1434. http://doi.org/10.1080/01431168608948945

Hunter, P. D., Gilvear, D. J., Tyler, a. N., Willby, N. J., & Kelly, A. (2010). Mapping macrophytic vegetation in shallow lakes using the Compact Airborne Spectrographic Imager (CASI). *Aquatic Conservation: Marine and Freshwater Ecosystems*, *20*(7), 717–727. http://doi.org/10.1002/aqc.1144

John W. Rouse, R.H. Haas, J.A. Schell, D.W. Deering, J. C. H. (1974). *Monitoring the vernal advancements and retrogradation of natural vegetation.* Greenbelt, MD, USA. Retrieved from http://ntrs.nasa.gov/archive/nasa/casi.ntrs.nasa.gov/19730017588.pdf (5th November, 2015)

Jones, K., Lanthier, Y., van der Voet, P., van Valkengoed, E., Taylor, D., & Fernández-Prieto, D. (2009). Monitoring and assessment of wetlands using Earth Observation: The GlobWetland project. *Journal of Environmental Management*, *90*(7), 2154–2169. http://doi.org/10.1016/j.jenvman.2007.07.037

Kiage, L. M., & Walker, N. D. (2009). Using NDVI from MODIS to monitor duckweed bloom in Lake Maracaibo, Venezuela. *Water Resources Management*, *23*(6), 1125–1135. http://doi.org/10.1007/s11269-008-9318-9

Kirkman, H. (1996). Baseline and monitoring methods for seagrass meadows. *Journal of Environmental Management*, *47*(2), 191–201. http://doi.org/10.1006/jema.1996.0045

Knipling, E. B. (1970). Physical and Physiological Basis for the Reflectance of Visible and Near-Infrared Radiation from Vegetation. *Remote Sensing of Environment*, *1*(3), 155–159. http://doi.org/10.1016/S0034-4257(70)80021-9

Köhler, J., Hachoł, J., & Hilt, S. (2010). Regulation of submersed macrophyte biomass in a temperate lowland river: Interactions between shading by bank vegetation, epiphyton and water turbidity. *Aquatic Botany*, *92*(2), 129–136. http://doi.org/10.1016/j.aquabot.2009.10.018

Kruse, F. A., Lefkoff, A. B., Boardman, J. W., Heidebrecht, K. B., Shapiro, A. T., Barloon, P.

J., & Goetz, A. F. H. (1993). The spectral image processing system (SIPS)—interactive visualization and analysis of imaging spectrometer data. *Remote Sensing of Environment*, *44*(2), 145–163. http://doi.org/10.1016/0034-4257(93)90013-N

Lee, Z., & Carder, K. L. (2004). Absorption spectrum of phytoplankton pigments derived from hyperspectral remote-sensing reflectance. *Remote Sensing of Environment*, *89*(3), 361–368. http://doi.org/10.1016/j.rse.2003.10.013

Lee, Z., Carder, K. L., Mobley, C. D., Steward, R. G., & Patch, J. S. (1999). Hyperspectral remote sensing for shallow waters. 2. Deriving bottom depths and water properties by optimization. *Applied Optics*, *38*(18), 3831–3843. http://doi.org/10.1364/AO.38.003831

Lee, Z. P., Du, K. P., Arnone, R., Liew, S. C., & Penta, B. (2005). Penetration of solar radiation in the upper ocean: A numerical model for oceanic and coastal waters. *Journal of Geophysical Research C: Oceans*, *110*(C9), 1–12. http://doi.org/10.1029/2004JC002780

Lee, Z., Weidemann, A., Kindle, J., Arnone, R., Carder, K. L., & Davis, C. (2007). Euphotic zone depth : Its derivation and implication to ocean-color remote sensing. *Journal of Geophysical Research: Oceans*, *112*(C3), 1–11. http://doi.org/10.1029/2006JC003802

Liira, J., Feldmann, T., Mäemets, H., & Peterson, U. (2010). Two decades of macrophyte expansion on the shores of a large shallow northern temperate lake — A retrospective series of satellite images. *Aquatic Botany*, *93*(4), 207–215. http://doi.org/10.1016/j.aquabot.2010.08.001

Liu, X. (2013). A Kernel Spectral Angle Mapper Algorithm for Remote Sensing Image Classification. In *Image and Signal Processing (CISP), 2013 6th International Congress* (pp. 814–818). IEEE. http://doi.org/10.1109/CISP.2013.6745277

Luo, J., Li, X., Ma, R., Li, F., Duan, H., Hu, W., … Huang, W. (2015). Applying remote sensing techniques to monitoring seasonal and interannual changes of aquatic vegetation in Taihu Lake, China. *Ecological Indicators*, *60*, 503–513. http://doi.org/10.1016/j.ecolind.2015.07.029

Ma, R., Duan, H., Liu, Q., & Arthur, S. (2011). Approximate bottom contribution to remote sensing re fl ectance in Taihu Lake , China. *Journal of Great Lakes Research*, *37*(1), 18–25. http://doi.org/10.1016/j.jglr.2010.12.002

Majozi, N. P., Salama, M. S., Bernard, S., Harper, D. M., & Habte, M. G. (2014). Remote sensing of euphotic depth in shallow tropical inland waters of Lake Naivasha using MERIS data. *Remote Sensing of Environment*, *148*, 178–189. http://doi.org/10.1016/j.rse.2014.03.025

Malthus, T. J., Ciraolo, G., & La Loggia, G. (1997). *Can biophysical properties of submersed macrophytes be determined by remote sensing? (No. CONF-970319--)*. Ann Arbor, MI (United States).

Maritorena, S., Morel, A., & Gentili, B. (1994). Diffuse reflectance of oceanic shallow waters: Influence of water depth and bottom albedo. *Limnology and Oceanography*, *39*(7), 1689–1703. http://doi.org/10.4319/lo.1994.39.7.1689

Matthews, M. W., Bernard, S., & Winter, K. (2010). Remote sensing of cyanobacteria-dominant algal blooms and water quality parameters in Zeekoevlei, a small hypertrophic lake, using MERIS. *Remote Sensing of Environment*, *114*(9), 2070–2087. http://doi.org/10.1016/j.rse.2010.04.013

Meehan, A. J., Williams, R. J., & Watford, F. A. (2005). Detecting trends in seagrass abundance using aerial photograph interpretation: Problems arising with the evolution of mapping methods. *Estuaries*, *28*(3), 462–472. http://doi.org/10.1007/BF02693927

Mobley, C. D. (2004). *Light and Water: Radiative transfer in natural waters (vol. 592)*. Academic press San Diego.

Morel, A. (1974). Optical Properties of Pure Water and Pure Sea Water. *Optical Aspects of Oceanography*, *1*, 1–24.

Mueller, J.L., Morel, A., Frouin, R., Davis, C., Arnone, R., Carder, K. et al. (2003). *Ocean Optics Protocols For Satellite Ocean Color Sensor Validation, Revision 4, Volume III: Radiametric Measurements and Data Analysis Protocols.* Greenbelt.

Nirmal Keshava and John F. Mustard. (2002). Spectral Unmixing. *IEEE Transactions on Signal Processing*, *19*(1), 44–57. http://doi.org/10.1109/79.974727

Orth, R.J., Wilcox, D.J., Nagey, L.S., Whiting, J.R., & Fishman, J. . (2000). *1999 Distribution of Submerged Aquatic Vegetation in the Chesapeake Bay and coastal bays*. Chesapeake Bay Program, Annapolis, MD. Grant No.CB993777-02-0. Retrieved from http://www.vims.edu/bio/sav/sav99 (5th December, 2015)

Oyama, K. (1993). Geographic differentiation among populations of Arabis serrata Fr. & Sav. (Brassicaceae). *Journal of Plant Research*, *106*(1), 15–24. http://doi.org/10.1007/BF02344368

Park, B., Windham, W. R., Lawrence, K. C., & Smith, D. P. (2007). Contaminant Classification of Poultry Hyperspectral Imagery using a Spectral Angle Mapper Algorithm. *Biosystems Engineering*, *96*(3), 323–333. http://doi.org/10.1016/j.biosystemseng.2006.11.012

Petzold, T. I. (1972). Volume Scattering Furctions for Selected Ocean Waters (No. SIO-REF-72-78). *Scripps Institution of Oceanography La Jolla Ca Visibility Lab*, 72–78. Retrieved from http://www.dtic.mil/cgi-bin/GetTRDoc?Location=U2&doc=GetTRDoc.pdf&AD=AD0753474 (8th December, 2015)

Pope, R. M., & Fry, E. S. (1997). Absorption spectrum (380-700 nm) of pure water. II. Integrating cavity measurements. *Applied Optics*, *36*(33), 8710–8723. http://doi.org/10.1364/AO.36.008710

Pu, R., Bell, S., Meyer, C., Baggett, L., & Zhao, Y. (2012). Mapping and assessing seagrass along the western coast of Florida using Landsat TM and EO-1 ALI/Hyperion imagery. *Estuarine, Coastal and Shelf Science*, *115*, 234–245. http://doi.org/10.1016/j.ecss.2012.09.006

Rulinda, C. M., Bijker, W., & Stein, A. (2010). Image mining for drought monitoring in eastern Africa using Meteosat SEVIRI data. *International Journal of Applied Earth Observation and Geoinformation*, *12*, S63–S68. http://doi.org/10.1016/j.jag.2009.10.008

Rybicki, N. B., & Landwehr, J. M. (2007). Long-term changes in abundance and diversity of macrophyte and waterfowl populations in an estuary with exotic macrophytes and improving water quality. *Limnology and Oceanography*, *52*(3), 1195–1207. http://doi.org/10.4319/lo.2007.52.3.1195

Salama, M. S., Dekker, A., Su, Z., Mannaerts, C. M., & Verhoef, W. (2009). Deriving inherent optical properties and associated inversion-uncertainties in the Dutch Lakes. *Hydrology and Earth System Sciences*, *13*(7), 1113–1121. http://doi.org/10.5194/hess-13-1113-2009

Salama, M. S., & Stein, A. (2009). Error decomposition and estimation of inherent optical properties. *Applied Optics*, *48*(26), 4947–4962. http://doi.org/10.1364/AO.48.004947

Schmidt, M., & Witte, C. (2010). Errata: Monitoring aquatic weeds in a river system using SPOT 5 satellite imagery. *Journal of Applied Remote Sensing*, *4*(1), 043528–043528. http://doi.org/10.1117/1.3459124

Sharma, A. R., Badarinath, K. V. S., & Roy, P. S. (2009). Comparison of ground reflectance measurement with satellite derived atmospherically corrected reflectance: A case study over semi-arid landscape. *Advances in Space Research*, *43*(1), 56–64. http://doi.org/10.1016/j.asr.2008.10.010

Shekede, M. D., Kusangaya, S., & Schmidt, K. (2008). Spatio-temporal variations of aquatic weeds abundance and coverage in Lake Chivero, Zimbabwe. *Physics and Chemistry of the Earth*, *33*(8), 714–721. http://doi.org/10.1016/j.pce.2008.06.052

Silva, T. S. F., Costa, M. P. F., Melack, J. M., & Novo, E. M. L. M. (2008). Remote sensing of aquatic vegetation: theory and applications. *Environmental Monitoring and Assessment*, *140*(1-3), 131–145. http://doi.org/10.1007/s10661-007-9855-3

Stankelis, R., Naylor, M., & Boynton, W. (2003). Submerged aquatic vegetation in the mesohaline region of the Patuxent estuary: Past, present, and future status. *Estuaries and Coasts*, *26*(2), 186–195. http://doi.org/doi: 10.1007/BF02695961

Tosserams, M., Backx, J., van der Melj, V., Dijkers, C., & Slager, H. (2001). *Delta Natural; Subproject for the research track Blue Delta, stone for the Integral Vision Delta waters*. Ministry of Transport, Public Works and Water Management.Rijkswaterstaat, the National Institute for Inland Water Management and Waste Water Treatment (RWS, RIZA). RIZA report 2001.016. Retrieved from http://www.vnsc.eu/uploads/2011/01/voorstudienatuurontwikkelingsplan.pdf (20th November, 2015) Originally in dutch

U.S.Environmental Protection Agency. (1997). EPA/600/R-97/072. Methods for the determination of chemical substances in marine and estuarine environmental matrices, 2nd edition. Washington, DC 20460: U.S.EPA.

USGS. (2015). RSR of Landsat 8 OLI. Retrieved December 24, 2015, from http://landsat.usgs.gov

Valley, R. D., Drake, M. T., & Anderson, C. S. (2005). Evaluation of alternative interpolation techniques for the mapping of remotely-sensed submersed vegetation abundance. *Aquatic Botany*, *81*(1), 13–25. http://doi.org/10.1016/j.aquabot.2004.09.002

Visser, F., Wallis, C., & Sinnott, A. M. (2013). Optical remote sensing of submerged aquatic vegetation: Opportunities for shallow clearwater streams. *Limnologica-Ecology and Management of Inland Waters*, *43*(5), 388–398. http://doi.org/10.1016/j.limno.2013.05.005

Withagen, L. (2000). *DELTA 2000: Inventory of current situation Delta Waters (RIKZ/2000.047)*. Zealand, The Netherlands. Retrieved from http://www.vliz.be/en/imis?persid=8888 (18th October, 2015) Originally in dutch.

Yuan, L., & Zhang, L. Q. (2008). Mapping large-scale distribution of submerged aquatic vegetation coverage using remote sensing. *Ecological Informatics*, *3*(3), 245–251. http://doi.org/10.1016/j.ecoinf.2008.01.004

Zhao, D., Jiang, H., Yang, T., Cai, Y., Xu, D., & An, S. (2012). Remote sensing of aquatic vegetation distribution in Taihu Lake using an improved classification tree with modified thresholds. *Journal of Environmental Management*, *95*(1), 98–107.

http://doi.org/10.1016/j.jenvman.2011.10.007

APPENDIX 1. NDVI MAPS OF BINNENSCHELDE LAKE

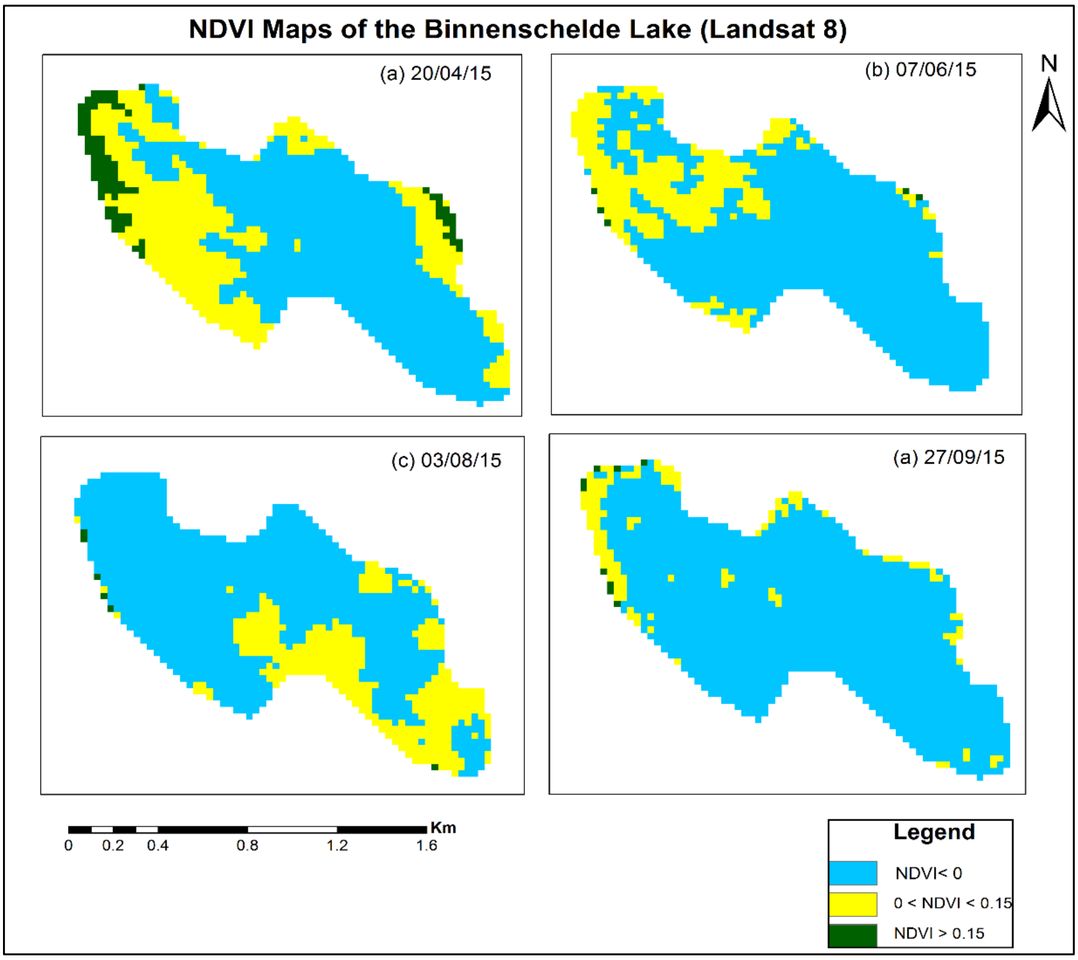

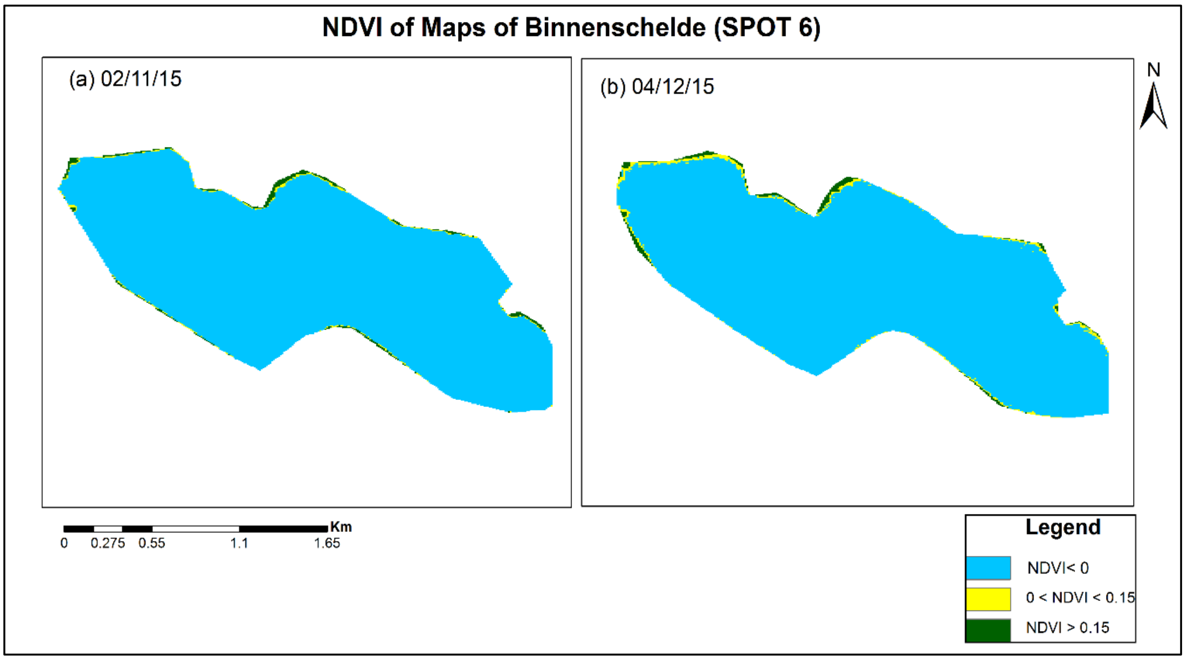

APPENDIX 2. ATMOSPHERIC CORRECTION

Uncorrected Landsat 8 image of 03/08/15 (4, 3, 2 band conbination)

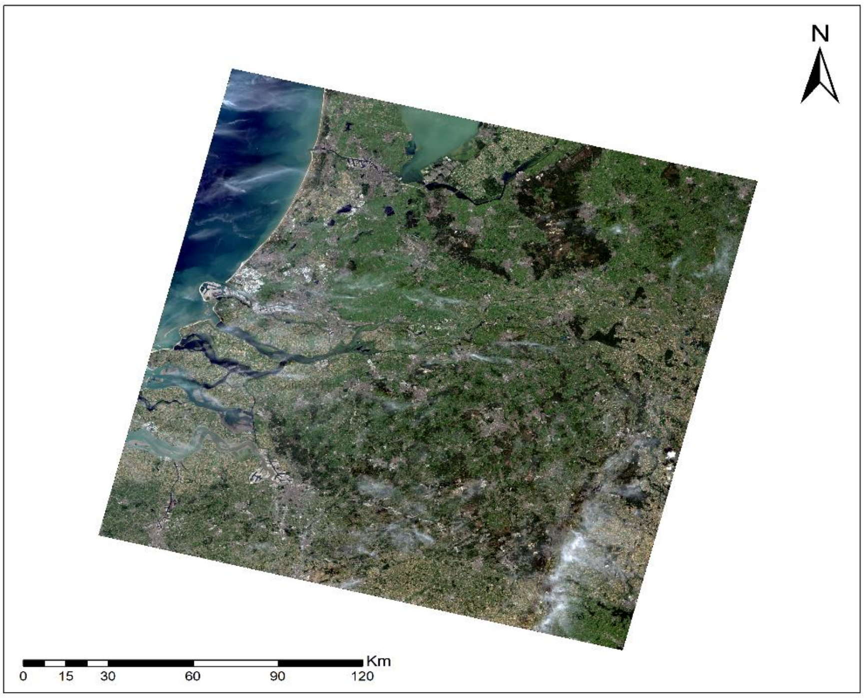

Atmospherically corrected Landsat 8 image of 03/08/15 (4, 3, 2 band combination)

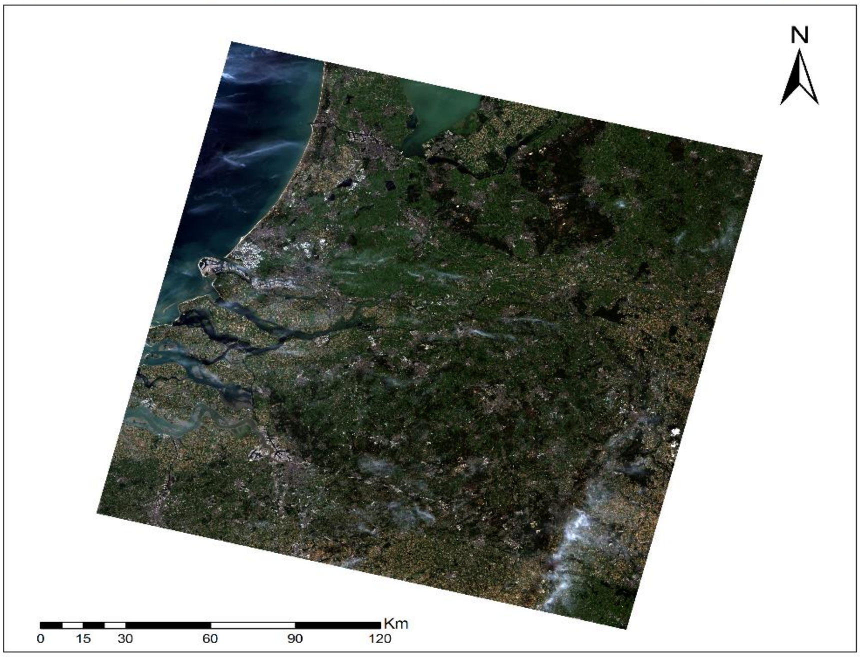

Uncorrected SPOT 6 image of 04/12/15 (3, 2, 1 band combination)

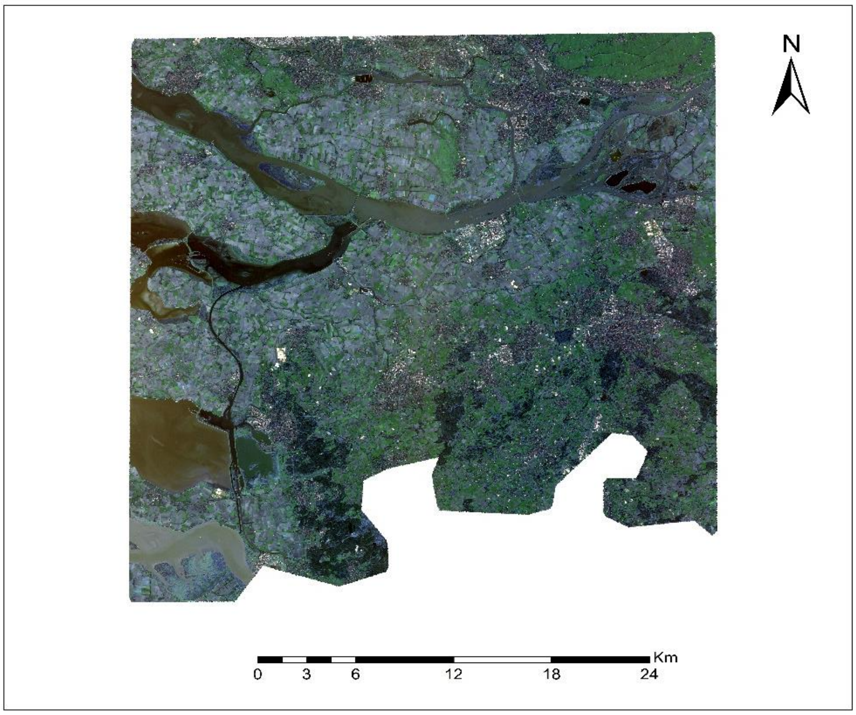

Atmospherically corrected SPOT 6 image of 04/12/15 (3, 2, 1 band combination)